Monthly Notices
of the
ROYAL ASTRONOMICAL SOCIETY

MNRAS **473,** 5591–5616 (2018)
Advance Access publication 2017 October 23

doi:10.1093/mnras/stx2719

A stellar census in globular clusters with MUSE: The contribution of rotation to cluster dynamics studied with 200 000 stars

S. Kamann,[1,2★] T.-O. Husser,[1] S. Dreizler,[1] E. Emsellem,[3,4] P. M. Weilbacher,[5] S. Martens,[1] R. Bacon,[4] M. den Brok,[6] B. Giesers,[1] D. Krajnović,[5] M. M. Roth,[5] M. Wendt[5,7] and L. Wisotzki[5]

[1]*Institute for Astrophysics, Georg-August-University, Friedrich-Hund-Platz 1, D-37077 Göttingen, Germany*
[2]*Astrophysics Research Institute, Liverpool John Moores University, 146 Brownlow Hill, Liverpool L3 5RF, UK*
[3]*ESO, European Southern Observatory, Karl-Schwarzschild Str. 2, D-85748 Garching bei München, Germany*
[4]*CRAL, Observatoire de Lyon, CNRS, Université Lyon 1, 9 avenue Ch. André, F-69561 Saint Genis-Laval Cedex, France*
[5]*Leibniz-Institute for Astrophysics (AIP), An der Sternwarte 16, D-14482 Potsdam, Germany*
[6]*Institute for Astronomy, Department of Physics, ETH Zürich, CH-8093 Zürich, Switzerland*
[7]*Institut für Physik und Astronomie, Universität Potsdam, D-14476 Potsdam, Germany*

Accepted 2017 October 15. Received 2017 October 15; in original form 2017 August 18

ABSTRACT

This is the first of a series of papers presenting the results from our survey of 25 Galactic globular clusters with the MUSE integral-field spectrograph. In combination with our dedicated algorithm for source deblending, MUSE provides unique multiplex capabilities in crowded stellar fields and allows us to acquire samples of up to 20 000 stars within the half-light radius of each cluster. The present paper focuses on the analysis of the internal dynamics of 22 out of the 25 clusters, using about 500 000 spectra of 200 000 individual stars. Thanks to the large stellar samples per cluster, we are able to perform a detailed analysis of the central rotation and dispersion fields using both radial profiles and two-dimensional maps. The velocity dispersion profiles we derive show a good general agreement with existing radial velocity studies but typically reach closer to the cluster centres. By comparison with proper motion data, we derive or update the dynamical distance estimates to 14 clusters. Compared to previous dynamical distance estimates for 47 Tuc, our value is in much better agreement with other methods. We further find significant ($>3\sigma$) rotation in the majority (13/22) of our clusters. Our analysis seems to confirm earlier findings of a link between rotation and the ellipticities of globular clusters. In addition, we find a correlation between the strengths of internal rotation and the relaxation times of the clusters, suggesting that the central rotation fields are relics of the cluster formation that are gradually dissipated via two-body relaxation.

Key words: techniques: imaging spectroscopy – stars: kinematics and dynamics – globular clusters: general.

1 INTRODUCTION

Over the last decades, dynamical studies have been a cornerstone to improve our understanding of Galactic globular clusters. Radial velocity measurements gave access to their velocity dispersions (Gunn & Griffin 1979; Pryor & Meylan 1993), revealed rotation (Meylan & Mayor 1986) and provided the first constraints on the binary fractions of the clusters (Pryor, Latham & Hazen 1988). Furthermore, the comparisons to theoretical models such as those of Michie (1963) or King (1966) allowed for the investigation of the internal structure of the clusters, for example by constraining mass segregation or inferring dynamical mass-to-light ratios (e.g. Da Costa & Freeman 1976; McLaughlin & van der Marel 2005). However, the high stellar densities inside globular clusters pose a problem to both observers and simulators. To observers, because of the challenges involved when performing spectroscopy in such dense environments, and to simulators, because of the high number of gravitational encounters that have to be considered during the lifetime of a cluster (e.g. Aarseth, Henon & Wielen 1974). Therefore, data–model comparisons were hampered by the simplifications of the models on the one hand and the sparsity of the data on the other hand for a long time.

Recent years saw a constant change as models became more and more realistic and observations produced steadily increasing sample sizes of stars per cluster. On the theoretical side, it became possible

★ E-mail: s.kamann@ljmu.ac.uk

© 2017 The Authors
Published by Oxford University Press on behalf of the Royal Astronomical Society

Downloaded from https://academic.oup.com/mnras/article-abstract/473/4/5591/4562634
by Liverpool John Moores University user
on 25 January 2018

to directly follow the evolution of clusters with realistic particle numbers in *N*-body models (e.g. Baumgardt & Makino 2003; Wang et al. 2016). Furthermore, Monte Carlo simulations allowed one to investigate the evolution of globular clusters for large parameter spaces and proved to yield results consistent with the more accurate *N*-body models (e.g. Giersz et al. 2013; Rodriguez et al. 2016). Finally, the ongoing work on analytical models has led to a more realistic handling of aspects such as rotation, anisotropy or mass segregation (Varri & Bertin 2012; Gieles & Zocchi 2015; Sollima et al. 2017).

On the observational side, the advent of integral-field spectrographs has enabled us to perform spectroscopy even in the crowded cluster centres (Noyola, Gebhardt & Bergmann 2008; Lützgendorf et al. 2011; Lanzoni et al. 2013; Kamann et al. 2014), while multi-object spectrographs allow for an efficient coverage of the outskirts of the clusters (Lane et al. 2011; Bellazzini et al. 2012; Lapenna et al. 2015). Thanks to high-precision astrometry, especially with the *Hubble Space Telescope* (*HST*), it became possible to measure proper motions around the cluster centres (Bellini et al. 2014; Watkins et al. 2015a), while the *Gaia* satellite promises to provide such information also for the outskirts of the clusters (Pancino et al. 2017).

Consequently, it is now possible to perform very detailed studies of the internal dynamics of Galactic globular clusters. One example in this respect is the quest for the origin of multiple populations that seem to be ubiquitous in globular clusters (e.g. Carretta et al. 2009; Milone et al. 2017). As shown by Renzini et al. (2015) or Bastian (2015), all the models used to explain the observed spreads in light element abundances have shortcomings. Studying the motions of the stars as a function of their chemical compositions can provide further insight. For example, Hénault-Brunet et al. (2015) argued that differences in the rotational patterns of the populations can be used to favour one model over the other. Though challenging, first attempts in this direction have been performed. Anisotropy variations across the various populations were detected by Richer et al. (2013) and Bellini et al. (2015) in 47 Tuc and NGC 2808, respectively. Recently, an enhanced rotational component of the extreme population in M13 was reported by Cordero et al. (2017).

In general, rotation is found to be quite common in globular clusters. Detailed studies revealing rotation were performed for a number of clusters, such as NGC 3201 (Cote et al. 1995), ω Centauri (van de Ven et al. 2006), M15 (van den Bosch et al. 2006), NGC 4372 (Kacharov et al. 2014), or recently for M53 (Boberg et al. 2017) and 47 Tuc (Bellini et al. 2017). In the surveys performed by Lane et al. (2010) or Bellazzini et al. (2012), rotation with amplitudes of a few $\mathrm{km\,s^{-1}}$ was uncovered in many clusters. The latter study also suggested a link between the rotation amplitude and the metallicities and horizontal branch morphologies of the clusters (but see Kimmig et al. 2015). Remarkably, all clusters studied by Fabricius et al. (2014) displayed rotation, the strengths of which correlated with the global ellipticities of the clusters. Such a correlation is not necessarily expected, given that the ellipticities of globular clusters are low compared to those of galaxies and that other mechanisms such as Galactic tidal forces (e.g. van den Bergh 2008) are likely to affect the appearance of globular clusters. Note that in contrast to previously mentioned studies, Fabricius et al. (2014) looked at the cluster centres, where relaxation times are shortest and rotation thus is most easily diminished by two-body interactions and the outward transport of angular momentum. Accordingly, models of rotating globular clusters are characterized by an increase of rotation amplitude with radius, up to a maximum that is located beyond the half-light radius (Lagoute & Longaretti 1996; Fiestas, Spurzem & Kim 2006; Varri & Bertin 2012; Jeffreson et al. 2017).

Despite the evidence for ordered motions, it is general consensus that all globular clusters are mainly supported by the random motions of their constituent stars. Analyses of the velocity dispersion profiles of the clusters have gained a lot of attention over the last years with regard to the question whether globular clusters harbour massive black holes. The results are still controversial (see the discussion in Lanzoni et al. 2013); however, the recent study of Baumgardt (2017) based on a large grid of *N*-body models and an extensive compilation of literature data suggests that intermediate-mass black holes are the exception rather than the rule in Galactic globular clusters. We emphasize that so far no intermediate-mass black hole has been unambiguously detected in a globular cluster. In clusters such as ω Centauri that appear as probable hosts because of their central kinematics, other effects such as radial anisotropies (Zocchi, Gieles & Hénault-Brunet 2017) or mass segregation of stellar remnants (Lützgendorf et al. 2013; Peuten et al. 2016) may mimic the signature of a massive black hole.

In this paper, we present the first results from a survey of 25 Galactic globular clusters observed with the integral-field spectrograph MUSE (Bacon et al. 2010). The instrument allows us to completely cover the cluster centres, out to approximately the half-light radii. Owing to the large stellar densities, the central regions are the most challenging ones for spectroscopic observations. In Kamann, Wisotzki & Roth (2013), we presented a method that allows us to deblend the spectra of overlapping stars and therefore to tap the full potential of integral-field spectrographs in crowded stellar fields. A pilot study of the globular cluster NGC 6397 was presented recently in Husser et al. (2016, hereafter Paper I) and Kamann et al. (2016, hereafter Paper II). It was based on 18 000 stellar spectra of 12 000 stars observed in less than one night of telescope time and illustrated the unique multiplexing capabilities of MUSE in crowded stellar fields and the prospects for studying the internal dynamics of globular clusters with these kinds of data. The promising results from this study lead us to conduct the survey that will be presented in the current paper.

This paper is organized as follows. In Section 2, we outline the design and the scientific aims of our globular cluster survey. The data reduction and analysis are presented in Sections 3 an 4. The internal dynamics of the sample clusters are presented in Section 5 and set into the scientific context in Section 6 before we conclude in Section 7.

2 THE MUSE SURVEY OF GALACTIC GLOBULAR CLUSTERS

As part of the MUSE guaranteed time observations, we are carrying out a survey of 25 globular clusters (PI: S. Dreizler). The clusters were selected to be nearby ($d < 15\,\mathrm{kpc}$), massive (central velocity dispersions $\sigma_c \gtrsim 5\,\mathrm{km\,s^{-1}}$) and well visible from Paranal. These criteria ensure short observing times and well-resolvable kinematics at the expected velocity accuracy of MUSE of $\gtrsim 1\,\mathrm{km\,s^{-1}}$ (cf. Paper II). For most clusters, we aim to completely cover the central regions, out to approximately their half-light radii. In a few clusters with large half-light radii, our coverage will remain incomplete given the large number of pointings that would be required to achieve a complete coverage. An overview of the clusters that are included in our survey and the number of pointings per cluster that were already observed is given in Table 1.

There are a variety of science cases that we plan to pursue with these data, ranging from the analysis of the cluster dynamics over

Downloaded from https://academic.oup.com/mnras/article-abstract/473/4/5591/4562634
by Liverpool John Moores University user
on 25 January 2018

Table 1. Overview of the globular clusters observed in the MUSE survey. (1) NGC number. (2) Alternative identifier (if any). (3) Number of pointings. This number roughly corresponds to the covered field of view in arcminutes. (4) Average number of epochs available for each pointing. (5) Total integration time in hours. (6) Number of extracted spectra. For clusters marked with an asterisk the analysis is still pending (see the text). (7) Number of stars with at least one extracted spectrum.

NGC	Name	$N_{\rm pointings}$	$N_{\rm epochs}$	ToT (h)	$N_{\rm spectra}$	$N_{\rm stars}$
(1)	(2)	(3)	(4)	(5)	(6)	(7)
104	47 Tuc	10	7	6.4	84 558	19 181
362		4	2	0.7	9530	6112
1851		4	4	2.2	24 600	9102
1904	M79	4	4.5	1.9	*	*
2808		4	2	1.2	13 762	6640
3201		4	8	5.8	27 190	4186
5139	ω Cen	10	4	4.9	63 747	27 390
5286		1	1	0.2	*	*
5904	M5	4	1	0.4	11 252	9639
6093	M80	3	1	0.7	5901	3929
6121	M4	2	1	0.1	1030	926
6254	M10	4	2.5	1.7	15 925	9071
6266	M62	4	2	1.1	14 555	11 129
6293		1	2	0.1	829	598
6388		4	4	2.2	32 942	12 334
6441		4	4	2.8	29 192	11 654
6522		1	2	0.2	2889	2205
6541		4	1	0.6	8757	7190
6624		1	1	0.2	*	*
6656	M22	4	1	1.2	14 234	10 272
6681	M70	1	2	0.8	5984	4036
6752		4	2	0.8	14 582	7362
7078	M15	4	2	1.1	16 068	10 420
7089	M2	4	4	2.4	25 757	10 881
7099	M30	4	3.5	2.6	21 566	7547
Total:		94	68.5	42.2	444 850	191 804

binary studies and chemical analyses to the search for emission-line sources. To enable a comprehensive search for binary stars, each cluster is observed in multiple epochs. The numbers of epochs per cluster that are currently available are included in Table 1. Note that the observations are still ongoing. For some clusters, we plan to obtain 15 epochs that will enable us to characterize the orbits of detected binaries. For the remaining clusters, we plan to complete three epochs that will be sufficient for the detection of binary stars. Analyses of the binary populations of the clusters will be presented in follow-up studies (Giesers et al., submitted). The same is true for the analysis of stellar parameters or emission-line stars. In addition, there is a huge legacy value of our survey as it represents the first blind spectroscopic survey of the central regions of globular clusters. Interesting objects such as optical counterparts to X-ray sources (e.g. Chomiuk et al. 2013), stars in unexpected locations of the colour–magnitude diagrams (like sub-subgiants; e.g. Mathieu et al. 2003; Geller et al. 2017), extremely low mass white dwarfs or gas clouds in direction of the clusters (Wendt et al. 2017) will be the subject of dedicated publications.

3 OBSERVATIONS AND DATA REDUCTION

For the current paper, we used all data that were observed before 2016 October. The data were observed during 14 observing runs (in visitor mode), starting in 2014 September. During each epoch, each targeted pointing was observed with three different instrument derotator angles (0, 90 and 180 degrees) in order to level out possible resolution differences between the individual spectrographs. All data were observed in the nominal mode without adaptive optics (AO), providing a continuous wavelength coverage from 4750 to 9350 Å. The full width at half-maximum of the MUSE line spread function is ∼2.5 Å and is approximately constant across the wavelength range, corresponding to a spectral resolution of $R \sim 1700$ at the blue and $R \sim 3500$ at the red end. The seeing (measured on the reduced data cubes) was typically good during the observations, with a median value of 0.74 arcsec and 95 per cent of the values in the range (0.48 arcsec, 1.10 arcsec).

The reduction of all cubes was carried out using the standard MUSE pipeline (Weilbacher et al. 2012, 2014). For each exposure, the basic steps of the reduction cascade (bias subtraction, tracing of the slices, wavelength calibration and basic science reduction) were performed in the *MuseWise* system developed within the MUSE GTO team (Vriend 2015). The outcome of these steps – 24 pixel tables, one per spectrograph – was checked for consistency. We found that a non-negligible fraction of the data (∼20 per cent) were compromised by inaccuracies in the wavelength calibration. These were detected by determining radial velocities for the telluric absorption bands across various regions of the field of view, which showed systematic shifts of several km s^{-1} between individual spectrographs. The origin of this issue could be traced back to the refinement of the wavelength solution derived from the calibration data using bright skylines in the science data. For short exposures $\lesssim 60$ s and dense clusters, the skylines were sometimes not visible because of the intensity of the starlight; hence, their centroids were measured with large inaccuracies. In version 1.6 of the pipeline, this problem was solved by removing the pixels with the strongest (stellar) signal via asymmetric kappa-sigma clipping and measuring the centroids of the skylines in the remaining pixels only. We reprocessed all exposures that were affected by this problem with the latest version of the pipeline and adapted the parameters of the kappa-sigma clipping such that the wavelength accuracy was sufficient across the whole field of view. Again, the radial velocities of the telluric absorption bands were used to verify that the offsets between the spectrographs had vanished.

In the next step of the data reduction process, the 24 pixel tables were flux calibrated and combined into a single pixel table. Finally, the three pixel tables created per epoch and pointing were combined and resampled into the final data cube on which we performed the further analyses. In total, we obtained 351 cubes. After a careful visual selection, 35 cubes were excluded from further analysis, either because of very bad seeing, clouds or artefacts of currently unknown origin. We did not perform any sky subtraction during the data reduction process because our fields do not contain any patches of empty sky, and the observation of dedicated sky exposures would have been too expensive observationally given the number of exposures. We deal with the night sky when extracting the spectra (cf. Section 4).

To illustrate the richness of the MUSE data, we show in Fig. 1 the collection of whitelight mosaics for all clusters of our sample, created by collapsing the cubes in spectral direction and combining the individual pointings using the SWARP software package (Bertin et al. 2002). Note that for NGC 104 and NGC 5139, we only show the central mosaics while omitting two and three individual pointings at larger distances to the cluster centre, respectively. In NGC 6121, which we only included as a backup target for bad seeing conditions, only two out of the four planned pointings have been observed so far. Apart from this, all planned pointings have been observed and reduced at least once.

Downloaded from https://academic.oup.com/mnras/article-abstract/473/4/5591/4562634
by Liverpool John Moores University user
on 25 January 2018

Figure 1. GRI mosaics of all observed clusters, created from the reduced MUSE data and ordered by increasing NGC number. Note that for NGC 104 (47 Tuc) and NGC 5139 (ω Centauri), two and three pointings, respectively, with larger distances to the cluster centres are not shown. In each mosaic, north is up and east is left.

4 DATA ANALYSIS

In large parts, the analysis of the data cubes was done in a similar way to our pilot study on NGC 6397. Details on the individual steps of the spectrum extraction and the spectral analysis can be found in Papers I and II. In the following, we restrict ourselves to a brief summary of both steps and put emphasis on new aspects that have been introduced since the publication of these papers.

4.1 Spectrum extraction

The extraction of the individual stellar spectra from the data cubes was performed with our dedicated software presented in Kamann et al. (2013). It determines the positions of the sources as well as the shape of the point spread function (PSF) as a function of wavelength and uses this information to optimally extract the spectrum of each resolved star. For this method to work, an input catalogue of sources is needed that provides astrometry and broad-band magnitudes across the MUSE field of view. Where possible, we used *HST* data from the Advanced Camera for Surveys (ACS) of Galactic globular clusters (Sarajedini et al. 2007; Anderson et al. 2008) as input. However, some of our clusters (NGC 1904, NGC 6266, NGC 6293, NGC 6522) were not included in the survey. In addition, our outer pointings in NGC 104 and NGC 5139 are located outside of the footprint of their ACS observations. In those cases, we obtained archival *HST* images and analysed them with the DOLPHOT software package (Dolphin 2000). An overview of the additional *HST* data that were used can be found in Table 2.

The spectra were extracted from the cubes in a multi-step process. First, the subset of sources from the input catalogue that is resolved at the lower spatial resolution of the MUSE data is identified. Using those, in a second step, a common PSF and a coordinate transformation from the input catalogue are fitted to the MUSE data. The wavelength dependences of those quantities are modelled as smooth functions of the wavelength afterwards. Finally, this information is used to extract all spectra. The number of spectra that could be extracted in this way varied with the seeing and the densities of the clusters and was typically between 1000 and 5000 stars per pointing.

In contrast to most spectroscopic surveys, we do not perform any pre-selection of the observed stars, but instead aim to obtain a spectrum of every star in the field of view. Consequently, spectra are extracted over a wide range of signal-to-noise ratios (S/N),[1] including many spectra for which the S/N is too low to perform any meaningful analysis. In a first cut, we exclude all spectra with $S/N < 5$ from any further analyses. This left us with about 813 000 spectra of about 273 000 stars. The cumulative histograms of the remaining spectra and stars are shown in Fig. 2. Note that the shape of the histograms, a steep rise at low S/N that gets shallower when moving to higher S/N, is a direct consequence of the luminosity function of the cluster stars. The number of stars per magnitude bin increases when moving to fainter magnitudes.

[1] As in Paper I, the S/N we provide is the average value for each extracted spectrum determined with the method of Stoehr et al. (2008).

Downloaded from https://academic.oup.com/mnras/article-abstract/473/4/5591/4562634
by Liverpool John Moores University user
on 25 January 2018

Table 2. Summary of archival *Hubble* data that were analysed in order to obtain source positions and magnitudes for pointings/clusters without coverage in the ACS survey of Sarajedini et al. (2007).

NGC	Camera	Filters	Proposal ID(s)	Comment
104	WFC3	*F225W*, *F336W*	12971	Only available for one of the two outer fields.
1904	WFPC2	*F336W*, *F439W*, *F555W*	6095, 6607	Used catalogue from Piotto et al. (2002).
5139	ACS	*F435W*, *F625W*	9442	
6266	WFC3	*F336W*	11609	
	WFPC2	*F336W*, *F439W*, *F555W*, *F814W*	8118, 8709	Used catalogue from Piotto et al. (2002).
6293	WFC3	*F390W*, *F555W*, *F814W*	12516	
6522	ACS	*F435W*, *F625W*	9690	

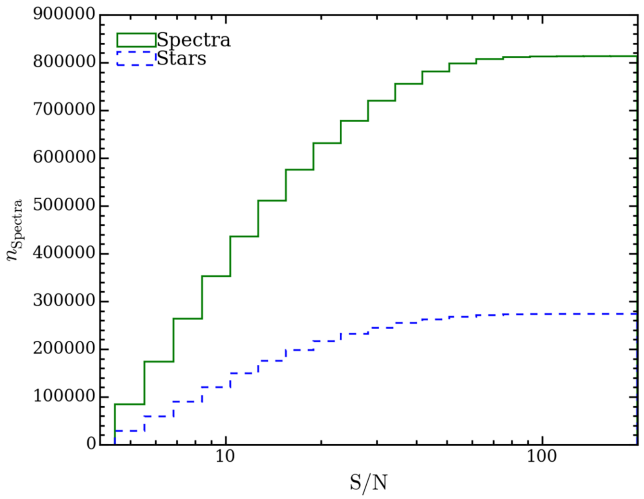

Figure 2. Cumulative S/N histogram of all spectra that were extracted from a data cube with S/N > 5 (solid green line) and of the highest S/N spectra that were extracted for individual stars (dashed blue line).

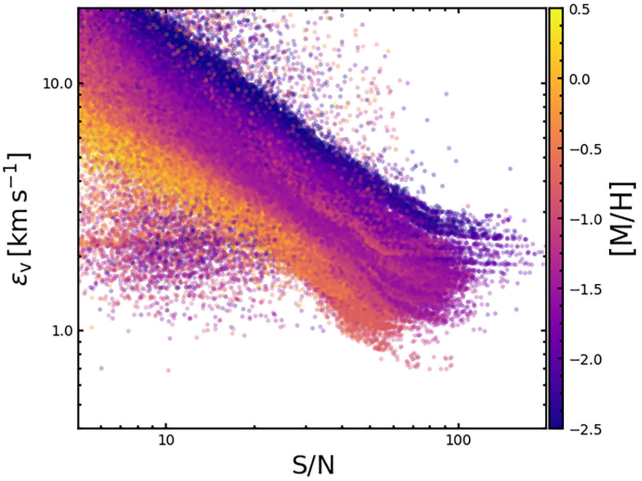

Figure 3. Calibrated uncertainties of the radial velocity measurements as a function of S/N of the spectra, colour-coded by and fitted metallicities.

4.2 Spectral analysis

The first step in the analysis of the extracted spectra was to obtain initial values for the stellar parameters of the corresponding stars using the photometric data. For each cluster, an isochrone from the PARSEC data base (Bressan et al. 2012) was fitted to the colour–magnitude diagram created from the *HST* data. Via a *8nearest-neighbour approach in colour–magnitude space, each star was assigned an initial guess for the effective temperature T_{eff} and the surface gravity $\log g$. The initial guesses for the metallicity $[M/\mathrm{H}]$ were chosen according to published values of the metallicities of the host clusters. Based on these values, a matching template from the Göttingen spectral library (Husser et al. 2013) was selected and an initial radial velocity was obtained via cross-correlation with the synthetic template. In the last step, a full-spectrum fit against the spectral library was performed to obtain final values for the radial velocity, the scaled solar metallicity and the effective temperature. The surface gravity was held constant at the initial value determined from the isochrone comparison because the spectroscopic determination of $\log g$ at the spectral resolution of MUSE is still an open issue. However, for the present study, this does not cause any problems.

For the analysis envisaged in this paper, it is fundamental that the radial velocities are reliable and their uncertainties are known precisely. We performed several checks and corrections to ensure this. As outlined in Paper I, the full-spectrum fit also includes a component that accounts for telluric absorption. In Paper II, we illustrated how this telluric component can be used to check the velocity accuracy across the field of view. For each cube, we selected all spectra with an S/N > 30 and obtained the radial velocities of the fitted telluric components. We then determined the mean telluric velocity and considered it as a measure for the absolute velocity offset of the cube. Hence, all stellar velocities determined from that cube were shifted by the mean telluric velocity. Similarly, we determined the standard deviation of the telluric velocities across the fields of view and considered it as a measure for the accuracy of the wavelength solution. This value was added quadratically to the uncertainties of the stellar radial velocities determined by the full-spectrum fit. In the last step, we compared the results obtained during different epochs for the same star. Under the assumption that the uncertainties are correct, the normalized velocity offsets should follow a normal distribution with a standard deviation of one. As in Paper II, we used this information to apply an additional correction as a function of the S/N of the spectra. Spectra of stars that showed obvious radial velocity variations were excluded from this comparison.

To give an idea of the accuracy of the radial velocities, we show the calibrated uncertainties ϵ_{v} as a function of S/N for all our clusters in Fig. 3. The data have been colour-coded by the metallicities derived from the spectra. As expected, the uncertainties strongly depend on the S/N of the spectra, with an average of $\epsilon_{\mathrm{v}} \approx 10\,\mathrm{km\,s^{-1}}$ at S/N = 10 and values accurate to 1–3 $\mathrm{km\,s^{-1}}$ for spectra with S/N $\gtrsim$ 50. The dependence of ϵ_{v} on metallicity can be easily explained by the weaker lines in spectra of low-metallicity stars. Note that these uncertainties are measured on individual *spectra* and that for most *stars*, more than one spectrum is already available. The

Downloaded from https://academic.oup.com/mnras/article-abstract/473/4/5591/4562634
by Liverpool John Moores University user
on 25 January 2018

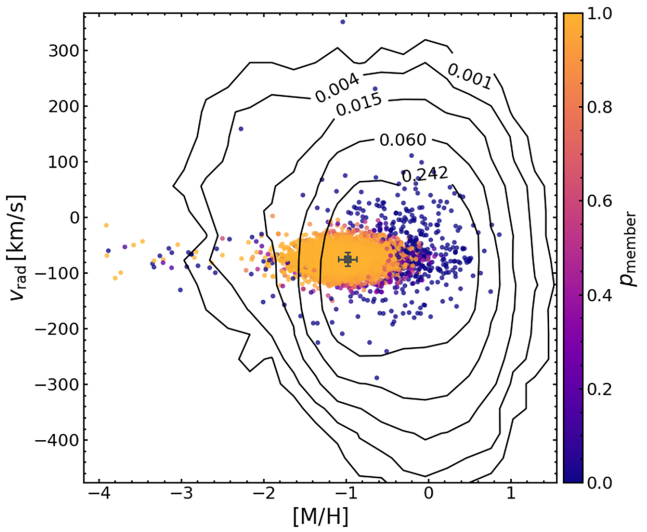

Figure 4. Membership probabilities of all stars observed towards NGC 6266 as a function of the measured metallicities and radial velocities. The contours show the density of expected Milky Way stars (in stars/arcmin^2/km s^{-1}/dex). The estimated mean velocity and metallicity of NGC 6266 and their estimated intrinsic spreads are indicated as a light grey square.

uncertainties of the averaged stellar velocities will decrease by $\sqrt{n}$ on average, with n the number of averaged spectra.

4.3 Cluster memberships

Given the large area on the sky covered by our MUSE data, our stellar samples will be contaminated by stars that are not cluster members. As in Paper II, we used a modified version of the expectation–maximization method presented by Walker et al. (2009) to separate cluster members and non-members in a homogeneous way. For the line of sight towards each cluster, we generated a realization of the contaminant population using the Besançon model of the Milky Way (Robin et al. 2003). The available photometry was used to constrain the list of simulated stars to the apparent magnitude range of our data. The simulation provided us with an expected distribution of the non-member stars in the radial velocity–metallicity plane towards each cluster. The expectation–maximization method was then used to compare the measurements of $[M/\mathrm{H}]$ and v_r of every star to the probability densities expected for the cluster and the non-member stars. Each star was assigned a probability of cluster membership such that the overall likelihood was maximized under the boundary condition that the fraction of cluster to non-member stars decreases monotonically with increasing distance to the cluster centre. For more details on the method, including the formulae that have been used, we refer to Walker et al. (2009) and Paper II.

The efficiency of the membership determination is illustrated in Fig. 4 for NGC 6266, a cluster that is prone to contamination by Milky Way stars because of the high surface density of Milky Way stars in its line of sight. The Milky Way model returns a broad metallicity distribution (indicated by the black contours in Fig. 4), with the metal-poorer part overlapping significantly with the cluster population in the v_r–$[M/\mathrm{H}]$ plane. Still the algorithm is able to identify the cluster population. Also visible in Fig. 4 is that the distribution of observed foreground stars nicely matches the distribution predicted by the Milky Way model, indicating the predictive power of the latter.

We considered all stars with $p_\mathrm{member} < 0.5$ as non-members. In total, this affected 4.1 per cent of our sample stars. As our sample includes clusters with different densities and in the bulge as well as in the halo of the Galaxy, the non-member fraction varied strongly, with the highest fraction of 32.0 per cent obtained for NGC 6522 and the lowest fraction of 0.4 per cent obtained for NGC 104. For the latter, contamination from the Small Magellanic Cloud (SMC) is also not an issue. The few apparent SMC stars we find in the sample have negligible membership probabilities because of the difference in radial velocities compared to NGC 104 ($-18.7\,\mathrm{km\,s^{-1}}$, SMC: $145.6\,\mathrm{km\,s^{-1}}$).

4.4 Selection of the final sample

Before performing any kind of analysis with data like ours, one has to define which subsample of stars is included in the analysis. This is always a trade-off between trying to exclude as many of the useless spectra (e.g. low S/N, strong cosmic ray hits, residuals from saturated neighbours) and avoiding to clip the sample by too much. In our case, we chose an S/N cut of 5 because it is the lower limit for trustworthy radial velocity measurements. However, even among the stars above this threshold, there will be some that suffer from one of the above problems. For example, the velocity measured from a spectrum with S/N = 20 can be strongly shifted by an undetected cosmic ray. As a visual inspection of all spectra is infeasible given our sample size, we introduced additional criteria to ensure that only reliable results enter the analysis of the cluster dynamics. These criteria are listed in the following.

(i) We made use of the circumstance that we have two independent measurements for the radial velocity determined from each spectrum. First, the reliability of each cross-correlation measurement was judged using the r-statistics as defined by Tonry & Davis (1979), and all spectra with $r < 4$ were clipped. Then, we determined the difference in radial velocities measured from the cross-correlation and the full-spectrum fit and only considered spectra where this difference was $<3\sigma$, with σ being the combined uncertainty of the two measurements.

(ii) In some cases, the full-spectrum fit returned unreasonably small uncertainties because of discontinuities in the χ^2 space. These stars are visible in the lower-right corner of Fig. 3. Such cases were also excluded.

(iii) Finally, we calculated broad-band magnitudes from the MUSE spectra and in the same passband that was used in the extraction process and calculated the differences Δm between input and recovered magnitudes. A large difference might indicate flux contamination from a nearby star or another problem. We defined a magnitude accuracy for each spectrum as $(1 + \Delta m/2\sigma_{\Delta\mathrm{m}})^{-2}$, where $\sigma_{\Delta\mathrm{m}}$ is the standard deviation of the magnitude differences of stars with comparable input magnitudes extracted from the same cube. Only spectra with an (empirically determined) magnitude accuracy >0.8 were accepted.

These selection criteria left us with 444 850 spectra of 191 804 stars. The numbers of spectra and stars for each individual cluster are provided in Table 1. Note that for three clusters (NGC 1904, NGC 5286 and NGC 6624), no numbers are provided. For those clusters, the spectral analysis was still pending when writing this paper because of problems with the isochrone fit. Hence, they have been omitted from the current analysis.

Finally, we removed stars with low probabilities of cluster membership ($p_\mathrm{member} < 0.5$, cf. Section 4.3) or that showed radial velocity variations. As mentioned earlier, binary studies are also foreseen

Downloaded from https://academic.oup.com/mnras/article-abstract/473/4/5591/4562634
by Liverpool John Moores University user
on 25 January 2018

with the MUSE data (Giesers et al., in preparation). They are still work in progress; however, we already have a preliminary binary probability for each star that was observed at least twice. We excluded stars with binary probabilities >0.5. We also verified that the results of the following analysis are not sensitive on which stars are excluded as binaries, likely because of the low overall binary fraction in globular clusters.

5 CLUSTER KINEMATICS

In order to study the dynamics of each cluster in a spatially resolved way, we applied two different binning schemes. First, we investigated the radial profiles by binning the stars according to their distances to the cluster centres. The radial bins were chosen such that each bin contained at least 100 stars and covered an annulus of $\log(r/\mathrm{arcsec}) \geq 0.2$. Secondly, we used the Voronoi tessellation code of Cappellari & Copin (2003) to create two-dimensional maps of the kinematics around the cluster centres. As the Voronoi binning code requires a regular grid as input, we pre-binned the data into quadratic cells of 3 arcsec × 3 arcsec size. The size of the Voronoi bins was chosen such that on average 100 stars were included in a bin.[2] Note that no weighting with luminosity, mass or S/N of the stars was applied when determining the Voronoi bins. Instead, each star was considered one measurement.

In each (radial or Voronoi) bin, we followed the maximum-likelihood approach introduced by Pryor & Meylan (1993) to obtain the dynamical properties. The method is based on the assumption that the probability of finding a star with a velocity of $v_i \pm \epsilon_i$ at projected distance r_i to the cluster centre can be approximated as

$$p(v_i, \epsilon_i, r_i) = \frac{1}{2\pi\sqrt{\sigma_\mathrm{r}^2 + \epsilon_i^2}} \exp\left\{\frac{(v_i - v_0)^2}{-2(\sigma_\mathrm{r}^2 + \epsilon_i^2)}\right\}, \quad (1)$$

where v_0 and $\sigma_\mathrm{r}(r_i)$ are the heliocentric radial velocity and the intrinsic dispersion profile of the cluster, respectively. A common approach for solving equation (1) that we follow here is to minimize the negative log-likelihood,

$$-\log\lambda = -\log\prod_{i=1}^{N} p(v_i, \epsilon_i, r_i) = -\sum_{i=1}^{N} \log p(v_i, \epsilon_i, r_i). \quad (2)$$

Equation (1) illustrates that it is crucial that the uncertainties, ϵ_i, of the radial velocity measurements are correct. Systematically underestimating the uncertainties would lead to an overestimate of the intrinsic velocity dispersion and vice versa. As outlined in Section 4.2, we used repeated measurements of the same stars to calibrate our uncertainties, so we believe they are accurate. Nevertheless, we will discuss the influence of the uncertainties on the dispersion curves below in Section 5.2.

One limitation of this approach is that it only strictly applies to stellar systems where the line-of-sight velocity distribution (LOSVD) can be described as a Gaussian of width $\sigma_\mathrm{r}(r_i)$, whereas rotation or higher moments of the LOSVD (e.g. h_3 and h_4 in the parametrization of van der Marel & Franx 1993) are neglected. As one of our aims in this work is to study cluster rotation, we extended the approach as outlined in the following. A common way to study the rotation of galaxies is *kinemetry* (Copin et al. 2001; Krajnović et al. 2006). It is based on the assumption that the variation of a kinematic quantity K (in our case, the mean velocity v_0) with position angle θ can be modelled as a harmonic expansion, i.e. as

$$K(r, \theta) = c_0(r) + \sum_{n=1}^{N} c_n(r)\cos\left[n(\theta - \phi_N(r))\right], \quad (3)$$

where the c_i and ϕ_i define the amplitudes and orientations of the individual components. The simplest case of a pure $n = 1$ cosine law corresponds to a rotating disc, whereas higher order moments quantify deviations from the disc model. As the rotation velocities expected in globular clusters are one to two orders of magnitude below those in galaxies, we restrict ourselves to the simple disc model. While there is no physical reason why globular clusters should behave as rotating discs, our assumption is justified by the observation that in galaxies – which typically have much more complex dynamics than globular clusters – the $n = 1$ term usually dominates (see Krajnović et al. 2005). This implies that we can study rotation in the radial bins by adding an angular dependence to the mean velocity of equation (1), i.e. by replacing

$$v_0 \longrightarrow \bar{v}(r_i, \theta_i) = v_0 + v_\mathrm{rot}(r_i)\sin(\theta_i - \theta_0(r_i)). \quad (4)$$

Here, $v_\mathrm{rot}(r)$ and $\theta_0(r)$ denote the projected rotation velocity and axis angle as a function of projected distance r to the cluster centre. The axis angle as well as the position angle θ_i of a star is measured from north through east. Note that according to equation (1), $\theta_0(r)$ is oriented such that the maximum (minimum) velocity is measured at $\theta_0 + \pi/2$ ($\theta_0 - \pi/2$).

Having all formulae at hand, we used the Markov chain Monte Carlo (MCMC) algorithm of Foreman-Mackey et al. (2013) to minimize $\log\lambda$ in every bin. For the four parameters we aimed to constrain per *radial* bin, we used constant probabilities across the following ranges as uninformative priors:

$$|v_0| < 1000\,\mathrm{km\,s^{-1}},\ \sigma_\mathrm{r} > 0\,\mathrm{km\,s^{-1}},\ v_\mathrm{rot} > 0\,\mathrm{km\,s^{-1}},\ 0 \leq \theta_0 < 2\pi.$$

In the cases where *Voronoi* binning was used, we enforced $v_\mathrm{rot} \equiv \theta_0 \equiv 0$ while keeping the same priors for v_0 and σ_r as in the radial binning scheme. Hence, we only obtained a mean velocity and a velocity dispersion in each Voronoi bin. However, rotation can still be studied by simply comparing the mean velocities between adjacent bins (see below). Compared to the radial bins, the Voronoi maps have the advantage that no assumptions about the rotation field are required. For both binning schemes, the uncertainties were estimated by running 100 chains with 500 steps each in which the parameters were varied slightly around their most likely values. The values we provide in the following are the median values and the 16th and 84th percentiles of the resulting parameter distributions.

In Fig. 5, we showcase the results from this analysis for three clusters from our sample. The results for the remaining clusters are displayed in Fig. A1 in Appendix A. In addition, all values from the analysis of the radial bins are provided in Table B1 in Appendix B.[3]

5.1 Rotation profiles

Thanks to the complete coverage of the central regions, the MUSE data are very well suited to investigate rotation in the clusters. A visual inspection of the radial profiles of v_rot or the Voronoi-binned maps of v_0 in Figs 5 and A1 reveals that many of the clusters

[2] Because of the low number of stars in NGC 6121 and NGC 6293, the number of stars per Voronoi bin was reduced to 50 and 30, respectively.

[3] The radial profiles are also made available as machine-readable data at https://musegc.uni-goettingen.de/.

Downloaded from https://academic.oup.com/mnras/article-abstract/473/4/5591/4562634
by Liverpool John Moores University user
on 25 January 2018

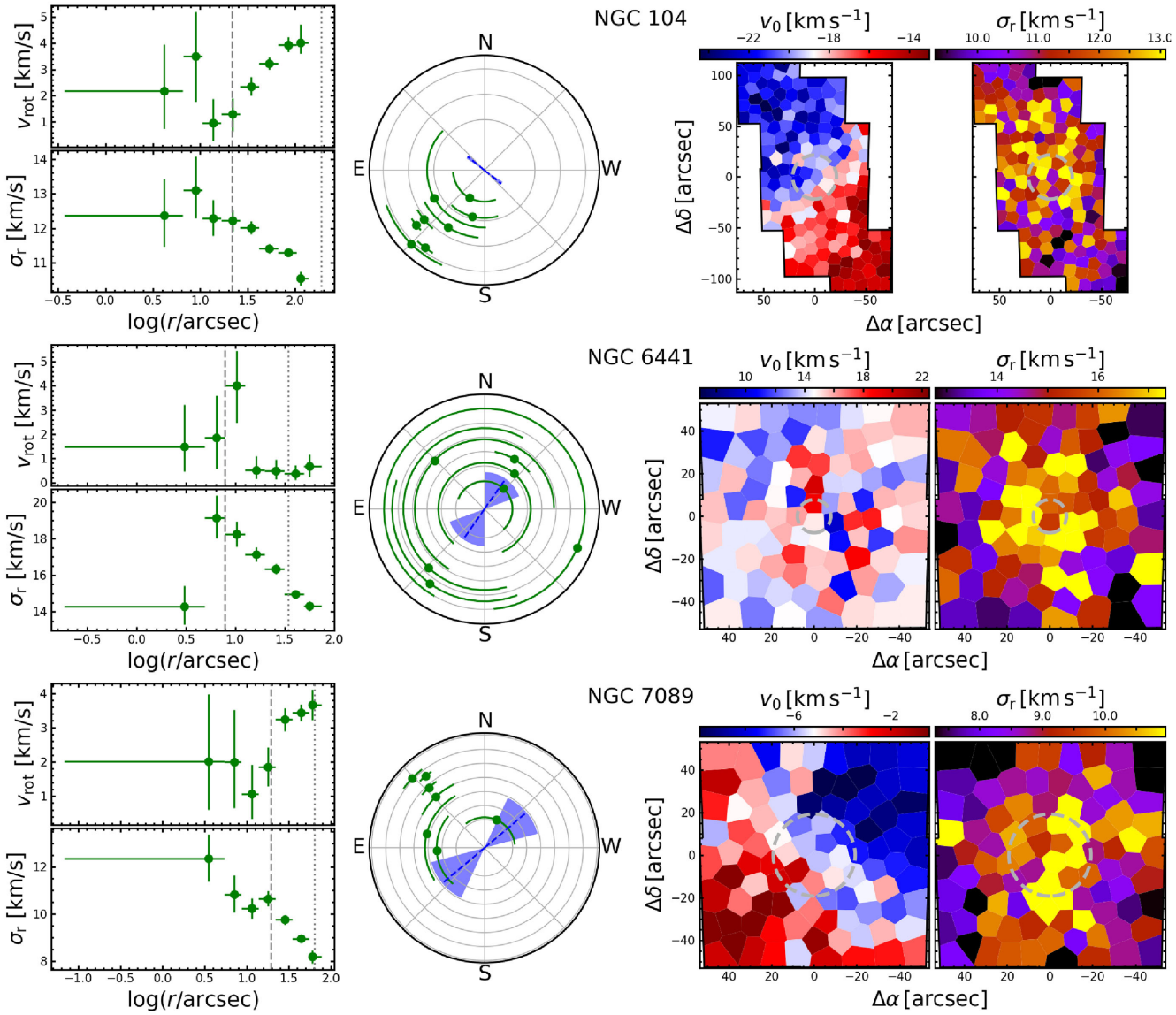

Figure 5. Results of the kinematic analysis for three clusters from our sample, NGC 104 (top), NGC 6441 (middle) and NGC 7089 (bottom). The left-hand panels show the radial rotation and dispersion profiles, respectively. The dashed and dotted vertical lines indicate the core and half-light radii of each cluster; all values were taken from Harris (1996). The central panel shows the position angle of the rotation curve and its uncertainty for each radial bin. A blue dashed line is used to indicate the cluster's photometric semi-major axis angle as determined in Section 6.1, with the blue shaded area indicating the uncertainty and the length of the line scaling with cluster ellipticity. The right-hand panels show Voronoi-binned maps of the mean velocity and the velocity dispersion across the footprint covered by the MUSE data. The dashed circles indicate again the core radii of the clusters. Similar plots for the remaining clusters of our sample are presented in Appendix A.

in our sample rotate. If we perform a visual classification of our sample into non-rotating or rotating clusters, we find that about 60 per cent (13/22) of the clusters show obvious rotation, while the remaining ones appear consistent with no rotation. Further inspection of the radial profiles of the rotating clusters reveals a pronounced similarity in that the rotation signal increases with distance to the cluster centre. It tends to disappear inside the core radius and steadily increases between the core and the half-light radius. This behaviour is in general agreement with the evolutionary globular cluster models of Fiestas et al. (2006) or the equilibrium models of Lagoute & Longaretti (1996) or Varri & Bertin (2012). It was also found in detailed studies of individual clusters like NGC 104 or NGC 5139 (e.g. Meylan & Mayor 1986; Merritt, Meylan & Mayor 1997; van de Ven et al. 2006; Sollima et al. 2009, see discussion below). Beyond the half-light radii, our data lack the radial coverage to investigate any further trends. In this respect, it is interesting to note that some of the clusters that we visually classified as non-rotating (NGC 3201, NGC 6121 and NGC 6254) have large core radii so that our data coverage is basically restricted to the areas inside the core radii. Hence, we cannot exclude the possibility that the clusters rotate at larger radii. This, and the fact that projection effects may also limit the amount of visible rotation in some clusters [the inclination of most clusters is not known, but see van de Ven et al. (2006) for NGC 5139 or Bellini et al. (2017) for NGC 104], leads us to conclude that the fraction of rotating clusters in our sample is probably significantly higher than 60 per cent.

Downloaded from https://academic.oup.com/mnras/article-abstract/473/4/5591/4562634
by Liverpool John Moores University user
on 25 January 2018

Table 3. Kinematic properties of the sample clusters as derived from the MUSE data. (1) NGC number. (2) Mean position angle of the rotation axis, measured from north to east. (3) Kinematic position angle (i.e. the direction of the positive rotation amplitude), determined from the Voronoi maps as described in the text. Note that for an easier comparison with $\langle\theta_0\rangle$, the kinematic position angles were offset by −90 deg. (4) Gradient of the rotation amplitude with increasing distance to the cluster centre. (5) Central velocity dispersion. (6) Effective stellar mass of the dynamic measurements. (7) Value of (v/σ) (cf. equation 5) measured at the half-light radius (or maximum radius covered by MUSE data in the cases where the half-light radius was not covered). (8) Value of λ_R (cf. equation 6) measured at the half-light radius or maximum radius covered by MUSE data. (9) Maximum radius covered by the MUSE data relative to the half-light radius of each cluster. (10) Dynamical distance, determined by comparison with the data of Watkins et al. (2015a).

NGC	$\langle\theta_0\rangle$ (deg)	$PA_{kin} - 90$ (deg.)	$\|\nabla v\|$ (km s^{-1} arcmin^{-1})	$\sigma_{r,0}$ (km s^{-1})	$m_{eff.}$ ($M_\odot$)	$(v/\sigma)_{HL}$	$\lambda_{R,HL}$	r_{max}/r_{HL}	$d_{Dyn.}$ (kpc)
(1)	(2)	(3)	(4)	(5)	(6)	(7)	(8)	(9)	(10)
104	134.1 ± 3.6	126.6 ± 7.1	2.9 ± 0.1	12.4 ± 1.0	0.78	0.17 ± 0.01	0.19 ± 0.01	0.58	4.4 ± 0.1
362	−42.0 ± 117.6		0.8 ± 0.3	7.7 ± 0.6	0.79	<0.04	<0.02	1.00	9.2 ± 0.8
1851	3.2 ± 3.5		2.0 ± 0.2	9.1 ± 0.8	0.81	0.08 ± 0.01	0.08 ± 0.01	1.00	10.8 ± 0.4
2808	−47.0 ± 2.4	−50.3 ± 8.1	4.8 ± 0.3	13.9 ± 1.1	0.82	0.13 ± 0.01	0.14 ± 0.01	1.00	9.6 ± 0.1
3201	−115.7 ± 188.9		0.4 ± 0.1	5.4 ± 0.5	0.70	<0.01	<0.01	0.49	
5139	9.9 ± 4.3	13.7 ± 3.6	1.8 ± 0.1	22.8 ± 1.9	0.71	0.17 ± 0.01	0.19 ± 0.01	0.54	5.2 ± 0.4
5904	−54.3 ± 20.3		2.2 ± 0.2	7.3 ± 0.8	0.79	0.14 ± 0.01	0.14 ± 0.01	0.84	6.9 ± 0.5
6093	−131.9 ± 18.0		3.0 ± 0.4	10.5 ± 0.8	0.78	0.06 ± 0.02	0.08 ± 0.01	1.00	
6121	−145.5 ± 9.4		1.2 ± 0.5	6.8 ± 0.7	0.73				
6254	142.8 ± 17.9		0.4 ± 0.1	5.6 ± 0.6	0.74	<0.01	<0.01	0.84	
6266	92.9 ± 21.8		1.4 ± 0.3	15.0 ± 1.1	0.80	0.03 ± 0.02	0.04 ± 0.00	1.00	6.2 ± 0.5
6293	−59.9 ± 15.0		5.9 ± 1.4	7.1 ± 0.7	0.77	0.19 ± 0.03	0.21 ± 0.02	0.82	
6388	−41.8 ± 16.8		1.5 ± 0.3	19.1 ± 1.4	0.89	<0.03	0.02 ± 0.01	1.00	11.0 ± 0.8
6441	−29.6 ± 20.8		0.7 ± 0.3	14.3 ± 1.1	0.92	<0.01	<0.01	1.00	12.5 ± 1.2
6522	−129.5 ± 163.6		2.6 ± 1.0	9.3 ± 0.9	0.79	<0.01	<0.01	0.91	
6541	−98.1 ± 5.1	−93.1 ± 12.7	3.1 ± 0.3	11.5 ± 1.1	0.75	0.14 ± 0.01	0.17 ± 0.01	1.00	
6656	−79.1 ± 23.9		1.1 ± 0.3	9.2 ± 0.9	0.69	0.03 ± 0.01	0.05 ± 0.01	0.47	3.5 ± 0.1
6681	98.7 ± 43.7		1.0 ± 0.4	8.4 ± 0.8	0.74	<0.03	<0.01	1.00	9.2 ± 1.2
6752	139.1 ± 41.8		0.5 ± 0.2	8.4 ± 0.7	0.73	<0.01	<0.02	0.74	4.2 ± 0.6
7078	150.9 ± 10.4		2.4 ± 0.3	14.0 ± 1.1	0.75	0.09 ± 0.01	0.10 ± 0.01	1.00	10.3 ± 1.7
7089	41.7 ± 2.7	38.1 ± 7.1	4.6 ± 0.2	12.3 ± 1.0	0.79	0.21 ± 0.01	0.22 ± 0.01	1.00	
7099	−115.4 ± 27.1		0.5 ± 0.2	8.1 ± 0.8	0.72	<0.01	<0.02	1.00	6.4 ± 0.5

From the radial profiles depicted in Figs 5 and A1, we inferred (variance-weighted) mean position angles of the rotation axes that are provided in Table 3. We also tried to infer the orientations of the rotation fields using the Voronoi maps that we created for the clusters. To this aim, we applied the method presented in appendix C of Krajnović et al. (2006). It works by creating a bi(anti)symmetric representation of a Voronoi map for various position angles and determining the position angle for which the difference to the actual Voronoi map is minimized (in a χ^2 sense). However, in the cases where the rotation velocity becomes comparable to the random velocity offsets per Voronoi bin (1–2 km s^{-1} in our case), the latter start to dominate the χ^2 statistics and the inferred position angle is poorly constrained (indicated by a 3σ uncertainty interval that covers almost the full circle). We discarded such measurements and provide in Table 3 the kinematic position angles only for the strongly rotating clusters that gave useful constraints. Note that the kinematic position angle points in the direction of the highest velocity (measured from north to east); hence, by definition it is offset by +90° from the axis angle θ_0. The comparison in Table 3 shows that in the cases where the 2D analysis was possible, the results for the two angles are in good agreement.

Central rotation in globular clusters was also studied by Fabricius et al. (2014) who detected a signal in all of the 10 (northern) targets of their sample. While also using integral-field spectroscopy, their approach to measuring rotation was completely different as they fitted a linear two-dimensional polynomial to the mean velocities measured in integrated light and obtained a velocity gradient and a rotation axis angle from the coefficients of the fit. In order to compare our results with Fabricius et al. (2014), we used again the radial profiles. By fitting a line to the rotational velocities as a function of projected distance r to the cluster centre and obtaining its slope, we obtained a velocity gradient $\|\nabla v\|$, which is provided in Table 3 for all clusters of our sample.

There are three clusters in common between our sample and the study of Fabricius et al. (2014): NGC 5904 ($\|\nabla v\| = 2.1 \pm 0.1 \pm 0.1$ km s^{-1}, $PA_{kin} = 58.5 \pm 2.8 \pm 5.6$ deg), NGC 6093 ($2.3 \pm 0.1 \pm 0.1$ km s^{-1}, $139 \pm 3.7 \pm 3.5$ deg) and NGC 6254 ($1.0 \pm 0.1 \pm 0.1$ km s^{-1}, $63.5 \pm 9.0 \pm 14.7$ deg), where the parentheses indicate their values for the velocity gradient and the kinematic position angle. When comparing position angles, note that Fabricius et al. (2014) again derived kinematic position angles and did not discriminate the senses of rotation; hence, their angles are offset by either +90° or −90° from our values. After accounting for these offsets, we find that despite the different approaches used, the results for the common cluster are in good agreement, and only the velocity gradients we derive for NGC 6093 and NGC 6254 are slightly higher and lower, respectively. A visual check of their velocity fields (their fig. 1) confirms that also the senses of rotation agree.

Larger samples of clusters have also been studied for rotation by Lane et al. (2010), Bellazzini et al. (2012), Lardo et al. (2015) and Kimmig et al. (2015). The first three studies follow on from one another and obtain similar conclusions; hence, we restrict ourselves to a comparison with the studies of Bellazzini et al. (2012) and Kimmig et al. (2015). However, any comparison is complicated because in contrast to our work, those studies focused on deriving

Downloaded from https://academic.oup.com/mnras/article-abstract/473/4/5591/4562634
by Liverpool John Moores University user
on 25 January 2018

global values for the clusters instead of rotation profiles. In addition, as the studies are based on multi-object spectroscopy, the majority of data were taken beyond the half-light radii of the clusters. We do find a general agreement in the sense that the clusters that show stronger rotation in the works of Bellazzini et al. (2012) and Kimmig et al. (2015) do so as well in our data. There is one notable exception though, which is NGC 6441. Bellazzini et al. (2012) and Kimmig et al. (2015) report rather high rotation amplitudes for this cluster (albeit with a large formal uncertainty in the latter study) whereas it is among the least rotating clusters in our sample (cf. Fig. 5). The strong rotational signal in the study of Bellazzini et al. (2012) is mainly caused by four stars at distances >5 arcmin to the cluster centre. As our data do not cover such large radii, it remains open whether this discrepancy is intrinsic to the dynamics of the cluster.

The clusters from our sample that have the most extensive literature data are NGC 104, NGC 5139 and NGC 7078. Bianchini et al. (2013) used these data to derive rotation profiles for all three clusters and found the rotation profiles to peak at distances $\sim$1.5$\times$ the half-light radii. They obtained global position angles of 136° (NGC 104), 12° (NGC 5139) and 106° (NGC 7078). While the former two are in excellent agreement with our values, a significant offset is observed for the latter one. However, Bianchini et al. (2013) also noted that for NGC 7078 the position angle changed with distance to the cluster centre, and decreased from an initial value of $\sim$260° inside the core radius to $\sim$100° when the entire radial velocity sample was used. This behaviour is in qualitative agreement with the results derived from the MUSE data (cf. Fig. A1). In addition, our data confirm the increase of the rotation velocity inside the core radius towards the cluster centre of NGC 7078 that was observed by Bianchini et al. (2013). These two features led van den Bosch et al. (2006) to conclude that NGC 7078 contains a decoupled core that might be a consequence of the late evolutionary stage of this core-collapsed cluster. We note that Bianchini et al. (2013) also report centrally increasing rotation for NGC 104 and NGC 5139, which is not confirmed by the MUSE data (cf. Figs 5 and A1). However, no uncertainties are given for the central rotation values of Bianchini et al. (2013); hence, the significance of this discrepancy remains unknown.

5.2 Dispersion and $V_{\rm rms}$ profiles

In the globular cluster literature, the velocity dispersion $\sigma_{\rm r}$ is often equated with the central second velocity moment $V_{\rm rms} = \sqrt{\sigma_{\rm r}^2 + v_{\rm rot}^2}$, implying that no rotation exists, i.e. $v_{\rm rot} \equiv 0$. While the analysis of the previous sections showed that the velocity dispersion is the dominant contribution to the second velocity moment in globular clusters, rotation should not be neglected. Hence, we will in the following distinguish between the velocity dispersion profiles provided in Figs 5 and A1 and the profiles of the central second velocity moment $V_{\rm rms}$, calculated according to the formula provided above.[4] The central velocity dispersions, $\sigma_{\rm r,0}$, for the sample clusters are provided in Table 3. They were determined as the weighted average of all dispersion measurements inside the core radius (or the value of the innermost bin in the cases where no bin fell into the core radius).

The $V_{\rm rms}$ profiles derived from the MUSE data are shown in Fig. 6 and show a range of radial dependences. In particular, we note that some clusters (NGC 362, NGC 6441 and NGC 6752) show a central dip in their profiles. While such a feature could be artificially caused by crowding effects – contamination by background light tends to bias the measured radial velocities towards the cluster mean – we do not think that this is the case. None of the clusters for which this effect is observed has a particularly steep surface brightness profile (see compilations by Trager, King & Djorgovski 1995 or Noyola & Gebhardt 2006) so the crowding towards the centre only increases moderately. On the other hand, clusters with very steep surface brightness profiles, such as NGC 7078 or NGC 7099, show the opposite behaviour with a central cusp. Such a cusp is also observed in NGC 3201 and NGC 5139, which instead have large core radii. The latter case deserves particular attention because of the ongoing controversy about an intermediate-mass black hole in its centre. Our central value of $V_{\rm rms} = 23.1^{+2.1}_{-1.7}\,{\rm km\,s^{-1}}$ lies above the models by Zocchi et al. (2017) without a black hole and is closer to the model of Baumgardt (2017) containing a black hole. However, dedicated modelling will be needed before drawing further conclusions.

Also included in Fig. 6 are the dispersion profiles from the compilation of literature data provided by Baumgardt (2017). A comparison to the MUSE data shows that for the vast majority of the clusters in common between the two samples, the profiles are in good agreement in the region where they overlap. Only in NGC 6121, and to a lesser extent also in NGC 3201, our second velocity moments are significantly larger than the literature values. We can think of two issues that could have artificially increased our profiles, undetected binaries or an underestimation of our velocity uncertainties. The impact of the latter increases as the velocity dispersion decreases; hence, it is suspicious that the offsets are observed for the two clusters with the lowest central velocity dispersion measurements in the literature. For NGC 6121, our analysis is based on two pointings without repeated observations; therefore, our uncertainty calibration is less certain than for the other clusters. However, NGC 3201 is among the clusters with the richest data sets (cf. Table 1), with on average seven repeated observations per star, making it unlikely that the uncertainties were systematically underestimated. In addition, our ongoing analysis of binary properties (Giesers et al., in preparation) suggests that in NGC 3201 all binaries with orbital velocities comparable to the cluster dispersion or higher are detected and removed from any further analysis. This is not the case for NGC 6121. Compared to more dense clusters, NGC 6121 has a relatively high binary fraction of 5–10 per cent in the core (Sommariva et al. 2008; Milone et al. 2012).

To check whether binaries might be responsible for the offset between our profile and the literature data, we used the code provided by Cottaar & Hénault-Brunet (2014, described in detail in Cottaar, Meyer & Parker 2012) to create stellar populations with the tabulated velocity dispersion of NGC 6121 and varying binary fractions. The distributions of mass ratios, log-periods and eccentricities were modelled as power laws, using the indices found by Kiminki & Kobulnicky (2012). We note that these distributions were obtained in a study of massive stars in OB associations. However, the corresponding values for globular clusters are poorly constrained observationally and therefore are a major source of uncertainty in the inferred binary fractions. We cut the period distribution at 100 years to take into account the low survival rates of wide binaries in the dense cluster environments. For simplicity, we further assumed a common mass of 0.8 $M_\odot$ for all observed stars. We then drew random samples from the distribution, assigned each star a velocity uncertainty that was randomly drawn from our observed sample and tried to recover the velocity dispersion using our maximum-likelihood approach. We found that on average, we overestimated the intrinsic velocity dispersion by 0.3 and 0.6 $\rm km\,s^{-1}$ for binary

[4] Note that our calculation of both quantities is based on the assumption that the velocity dispersion is Gaussian.

Downloaded from https://academic.oup.com/mnras/article-abstract/473/4/5591/4562634
by Liverpool John Moores University user
on 25 January 2018

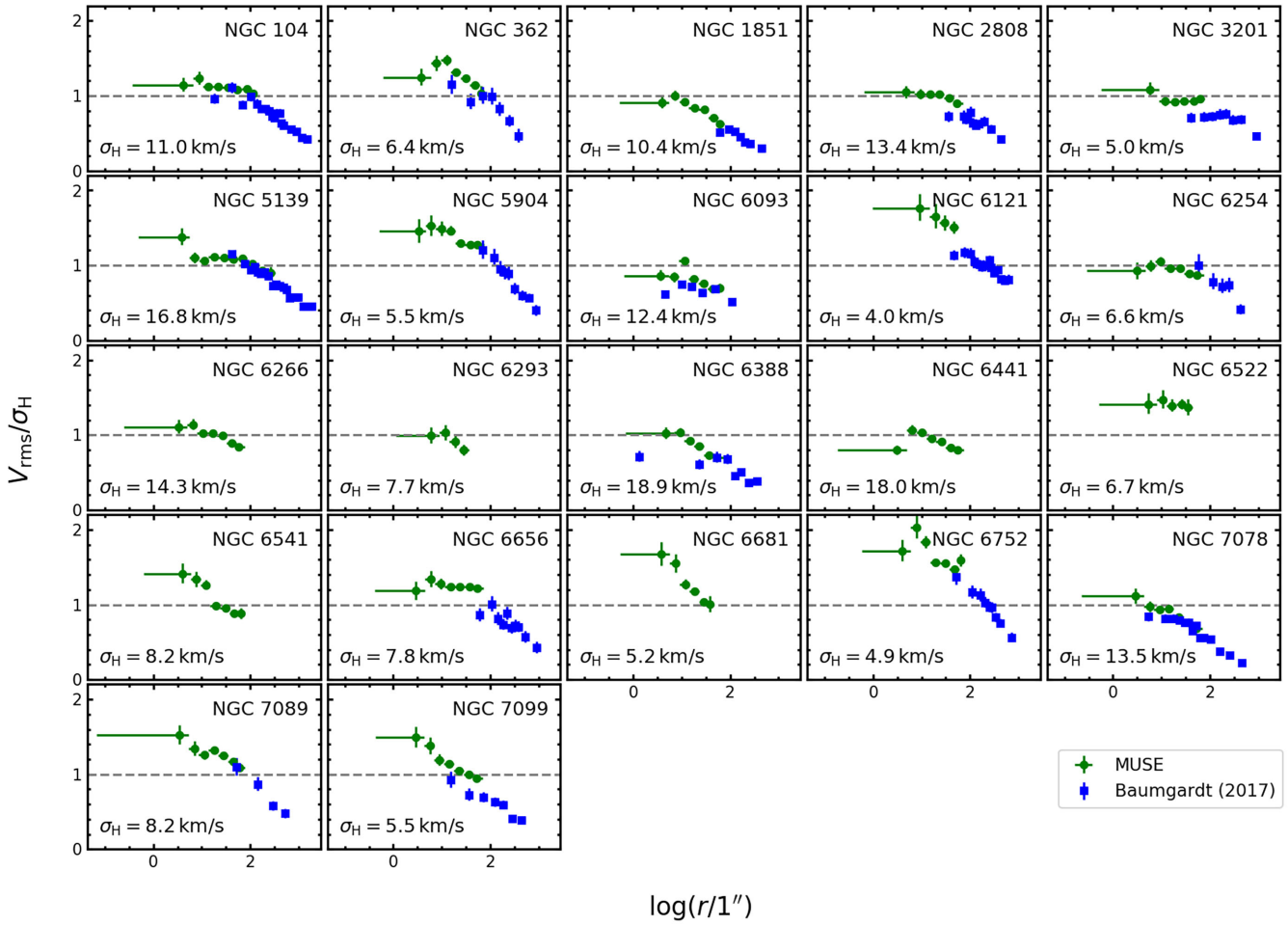

Figure 6. Comparison of the profiles of the second velocity moment determined from the MUSE data (green circles) and the literature compilation of Baumgardt (2017, blue squares). For clarity, each profile has been normalized to the central velocity dispersion provided by Harris (1996), the value of which is provided in the lower left of each panel.

fractions of 5 per cent and 10 per cent, respectively. Hence, while binaries may be responsible for part of the discrepancy, it is unlikely that they are the sole explanation.

Mass segregation may provide a physical explanation for the observed offset in NGC 3201 and NGC 6121. The literature profiles are based mainly on giant stars whereas the bulk of our sample in those two clusters consists of less massive main-sequence stars. We used our isochrone fits to obtain giant masses as well as effective masses for our samples. Effective masses were determined by calculating the weighted means of the masses of all stars that entered our analysis. The weight for each star was calculated as $1/(\sigma_r^2 + \epsilon_i^2)$, where σ_r^2 is the intrinsic dispersion at the position of the star and ϵ_i is the uncertainty of its final velocity measurement. As evident from equation (1), the weights take into account that stars with poorly determined velocity provide less stringent constraints on the measured likelihoods. In Table 3, the effective weights are listed for all of our clusters. For NGC 3201 and NGC 6121, we find 0.70 and 0.73 $M_\odot$, respectively. The giant masses in both clusters are $\sim$0.85 $M_\odot$. According to the model of Bianchini et al. (2016), the mass differences would correspond to a difference of $\lesssim$5 per cent in the velocity dispersion, which is smaller than the observed difference. However, when we split up the sample of NGC 3201 into five mass bins as shown in Fig. 7, the dispersion

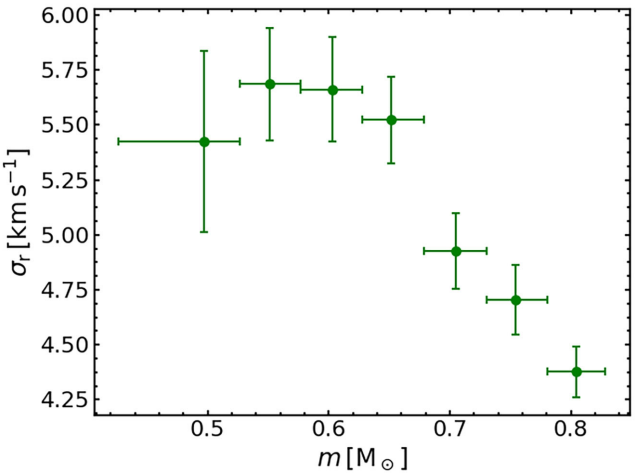

Figure 7. Velocity dispersion of the globular cluster NGC 3201, measured across the full MUSE mosaic and for different bins in stellar mass of the probed stars.

Downloaded from https://academic.oup.com/mnras/article-abstract/473/4/5591/4562634
by Liverpool John Moores University user
on 25 January 2018

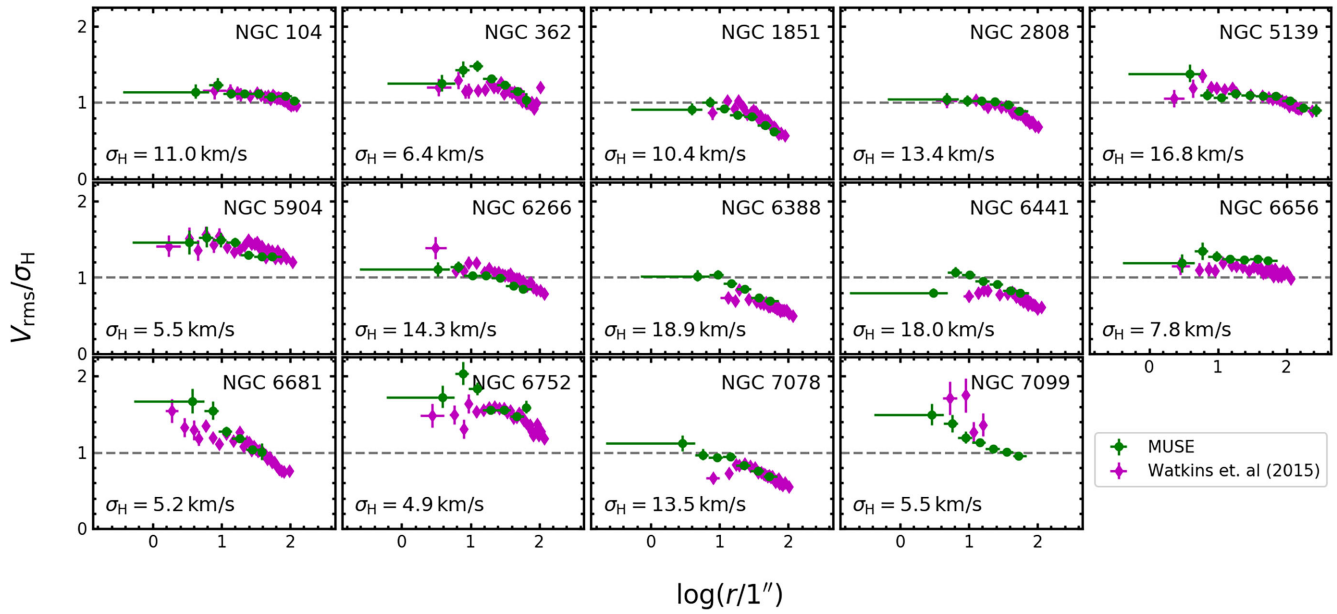

Figure 8. Comparison of the profiles of the second velocity moment determined from the MUSE data (green circles) and the proper motion data of Watkins et al. (2015a, purple diamonds) for clusters present in both samples. As in Fig. 6, the profiles have been normalized to the central dispersion values of Harris (1996) that are provided in each panel. The distances used to convert the proper motion profiles to km s^{-1} were also taken from Harris (1996).

increases towards lower masses and the value that we obtain for the highest mass bin is in good agreement with the literature data. We sound a note of caution that such an analysis of the mass-dependent kinematics is very challenging because lower masses correspond to lower luminosities and hence higher uncertainties of the measured radial velocities. So even small inaccuracies in the determination of the uncertainties can change the observed trend. For this reason, we postpone a dedicated study on mass segregation to a future publication. However, to facilitate a comparison of models to our data, we provide effective masses also for all of our radial bins in Table B1.

Five clusters from our sample are missing in the compilation of Baumgardt (2017) for which no dedicated radial velocity studies have been carried out so far.[5] For those clusters, our work provides the first detailed analysis of the cluster kinematics using radial velocities.

We also compared the profiles of the second velocity moment to the proper motion data of Watkins et al. (2015a) for the 14 clusters present in both samples. To convert the proper motion measurements from mas yr^{-1} to km s^{-1}, we used the cluster distances from Harris (1996). As can be seen from Fig. 8, the profiles are generally in good agreement. For some of the denser clusters (especially NGC 6388, NGC 6441 and NGC 7078), there is a trend of higher central values in the MUSE profiles compared to the proper motion profiles. The origin of this discrepancy is currently not clear. It occurs in the regions with the highest crowding, which can potentially affect both types of measurement. Therefore, a detailed comparison of the individual stellar velocities would be very helpful.

[5] In addition, no comparison data for NGC 6266 is shown in Fig. 6. The cluster was studied by Lützgendorf et al. (2013) using integrated-light spectroscopy instead of individual radial velocities. A comparison between these two approaches is foreseen at a later stage.

5.3 v/σ and λ_R profiles

The ratio between rotation and dispersion, hereafter referred to as (v/σ), is commonly used to evaluate the importance of rotation to the overall cluster dynamics. However, in the globular cluster community, no well-defined method has been established on how to measure (v/σ). Commonly, an overall rotation amplitude is measured for the observed radial range and compared to the central velocity dispersion of the cluster. This approach is comparable to the calculation of the ratio between the maximum rotation velocity and the central dispersion that has been used a while ago for galaxy analyses. Binney (2005) mentioned the weaknesses of this approach and proposed an enhanced treatment that has subsequently been used by the SAURON project (e.g. Cappellari et al. 2007; Emsellem et al. 2007). It is particularly well suited for integral-field data as it uses the entire footprint of an observation (typically after Voronoi binning the data) instead of only individual values. In this formalism, (v/σ) is calculated as (see Cappellari et al. 2007, equation 10)

$$\left(\frac{v}{\sigma}\right)^2 = \frac{\langle v^2\rangle}{\langle \sigma_r^2\rangle} = \frac{\sum_{n=1}^{N} F_n v_n^2}{\sum_{n=1}^{N} F_n \sigma_{r,n}^2}, \tag{5}$$

where the sum is over all Voronoi bins and F_n denotes the flux per Voronoi bin. The velocity v_n is measured relative to the systemic velocity of the object. As noted by Emsellem et al. (2007), a potential shortcoming of the (v/σ) value determined this way is that similar values may be obtained for objects with very different velocity fields. For this reason, they introduced the λ_R parameter, calculated as

$$\lambda_R = \frac{\langle r|v|\rangle}{\langle r\sqrt{v^2+\sigma_r^2}\rangle} = \frac{\sum_{n=1}^{N} r_n F_n |v_n|}{\sum_{n=1}^{N} r_n F_n \sqrt{\sigma_{r,n}^2 + v_n^2}}. \tag{6}$$

Downloaded from https://academic.oup.com/mnras/article-abstract/473/4/5591/4562634
by Liverpool John Moores University user
on 25 January 2018

In this case, r_n is the projected distance of a Voronoi bin to the object centre. Emsellem et al. (2007) showed that λ_R is a proxy for the spin parameter and that it provides a clear distinction between galaxies that show large-scale rotation and those that do not. The simulations of Jesseit et al. (2009) further showed that λ_R is a robust tracer for the true angular momentum content of galaxies.

Both approaches use the integrated fluxes F_n as a proxy for the stellar masses contained in each Voronoi bin. We obtained integrated fluxes by summing up the luminosities of the stars that fell in each Voronoi bin. To avoid biases because of incompleteness of the catalogues in the central regions, we only considered stars brighter than a given magnitude cut above which we considered the catalogue to complete. This limit was found to be in the range $V = 18$–20, depending on the cluster under consideration. We verified that the results were not sensitive on the chosen cut.

In principle, we could just run the formalism on our data, using the Voronoi maps of v and σ created for each of the clusters. However, a complication when working with globular clusters instead of galaxies is that the internal velocities are lower by one to two orders of magnitude. As visible from equations (5) and (6), both values are prone to biases if the random variations in v_n due to the measurement uncertainties are comparable to the variations because of rotation. For this reason, we developed a method to estimate the strength of the bias for our data and correct for it. It is outlined in Appendix C (see also appendix B in Emsellem et al. 2007).

To minimize the impact of uncertainties in the bias correction on our results, we decided to create new maps from the radial profiles instead of using the existing ones. The assumption of a cosine law in each radial bin helps to level off bin-to-bin variations and hence decreases the random velocity offsets per bin. To create two-dimensional maps from the radial profiles, we first calculated Voronoi bins of equal brightness from our photometric catalogues. For each bin, we then determined a mean velocity and a velocity dispersion from the radial profile of the given cluster. The errors from the radial bins were accordingly propagated to the Voronoi bins. In this way, we obtained Voronoi maps with strongly reduced velocity uncertainties per bin. Consequently, the values we obtained for (v/σ) and λ_R were less affected by biases and the corrections we had to apply were smaller (see Fig. C1 in Appendix C).

As Emsellem et al. (2007) showed, the values for (v/σ) and λ_R should be closely linked and follow the relation

$$\lambda_R = \frac{\kappa\,(v/\sigma)}{\sqrt{1+\kappa^2\,(v/\sigma)^2}}\,. \tag{7}$$

We found that our data were well reproduced by this relation with $\kappa = 1.1 \pm 0.1$, in good agreement with the values determined by Emsellem et al. (2007) for observed galaxies and two-integral Jeans models. Therefore, we will restrict ourselves to a discussion of the λ_R profiles in the following. We show an overview of the λ_R profiles obtained for the clusters in our sample in Fig. 9. The values of λ_R at the half-light radius (or at the maximum radius for clusters where the half-light radius is beyond the radial range covered by the MUSE data) are also provided in Table 3. We will use these values as measurements for the rotational support of the individual clusters in the discussion below. For completeness, we also included the values of (v/σ) at the half-light/maximum radii in Table 3.

The profiles shown in Fig. 9 confirm the visual impressions from Figs 5 and A1 in the sense that clusters where the rotation field was already visible by eye also show the steepest λ_R profiles. Among the clusters with the strongest rotational support in our sample are NGC 104, NGC 5139, NGC 6541 and NGC 7089. On the other hand, NGC 6441 and NGC 7099 seem to have barely any rotational support.

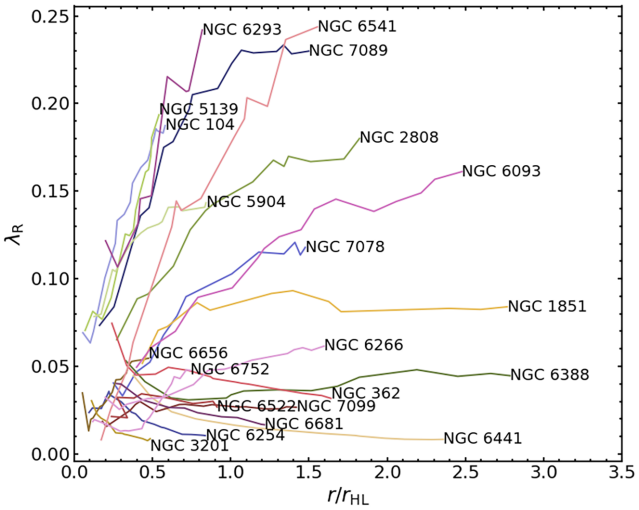

Figure 9. The λ_R profiles for the clusters from the MUSE sample. The radii have been normalized to the half-light radius of each cluster, taken from Harris (1996). Due to the limited coverage of the MUSE data of NGC 6121, the cluster was excluded from this comparison (see the text).

While the curves depicted in Fig. 9 show a variety of shapes, a common behaviour seems to be an almost linear increase of λ_R out to approximately the half-light radius and a flattening beyond that. This behaviour reflects the increase in rotation velocity that we observe for the majority of our sample. We will revisit the λ_R analysis below when we discuss rotation in connection with other properties of the clusters.

5.4 Dynamical distances

The availability of both radial velocity and proper motion profiles also enables the determination of dynamical distances for a subsample of our clusters. To this aim, we determined the radial ranges common to both studies and interpolated the proper motion profiles to the same binning as the MUSE profiles. For each bin, the ratio of the two values was determined and converted to a distance. Finally, the weighted mean of the distances determined in the individual bins was used as the distance to the cluster, while the standard deviation between the bins was used as uncertainty of the distance measurement. A comparison of the dynamical distances to the values of Harris (1996) is shown in Fig. 10; our values are also listed in Table 3. We found a mean value of the distance ratios of 0.99 ± 0.01, indicating an excellent agreement with the literature data. Three clusters show significant ($>2\sigma$) deviations from a 1:1 relation, namely NGC 1851, NGC 6656 and NGC 7099. NGC 7099 has the least amount of proper motion data, limiting the reliability of our measurement. The other two clusters will be discussed below.

Dynamical distances have also been determined by Watkins et al. (2015b) and Baumgardt (2017) who also found good agreement with the literature data, although the distances determined by Baumgardt (2017) were on average 8 per cent lower. There are two clusters for which our distances deviate significantly from the values determined by Watkins et al. (2015b) and Baumgardt (2017), NGC 104 (4.5 ± 0.1 kpc compared to 4.15 ± 0.08 kpc and 3.95 ± 0.05 kpc) and NGC 6656 (3.5 ± 0.1 kpc compared to 2.84 ± 0.16 kpc and 2.66 ± 0.10 kpc). For NGC 104, our measurement is in better agreement with other methods (e.g. Woodley et al. 2012). As the same

Downloaded from https://academic.oup.com/mnras/article-abstract/473/4/5591/4562634
by Liverpool John Moores University user
on 25 January 2018

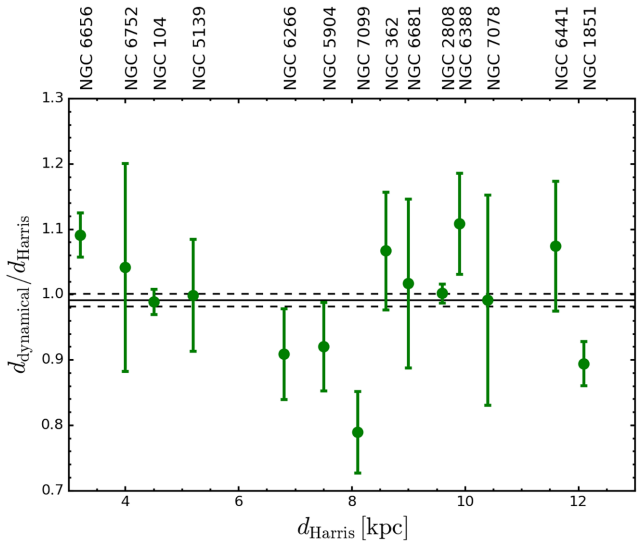

Figure 10. Ratio of the dynamical distances determined by matching the proper motion profiles of Watkins et al. (2015a) to the MUSE data and the distances in Harris (1996), as a function of the latter. The mean ratio and its uncertainty are indicated by the solid and dashed lines, respectively. The name of each cluster is provided at the top of the figure.

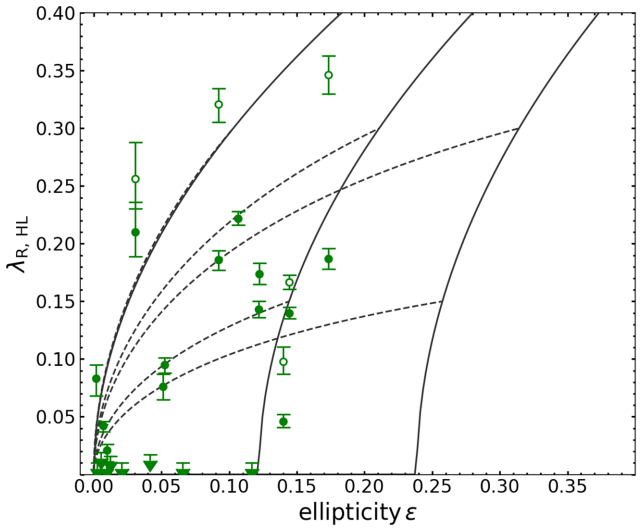

Figure 11. Rotation strengths as a function of the global ellipticities of the clusters, using $\lambda_{\rm R}$ as a measure of the importance of rotation. The $\lambda_{\rm R}$ values have been calculated at the half-light radius $r_{\rm HL}$ where possible, otherwise at the maximum radius covered by the MUSE data. In the latter cases, we also show the values obtained by linear extrapolation to $r_{\rm HL}$ as open symbols. The ellipticities have been taken from Harris (1996). The solid lines show the prediction for an edge-on oblate rotator in the isotropic case and for anisotropies of $\beta = 0.1$ and 0.2 [from left to right, using the formulae of Cappellari et al. (2007) and Emsellem et al. (2007)]. The dashed lines indicate the behaviour expected when varying the inclination.

proper motion data are used in all three studies, this suggests that the existing radial velocity dispersion data lead to an underestimation of the true distance of NGC 104. As argued by McLaughlin et al. (2006) or Bogdanov et al. (2016), this is probably caused by a bias of the existing radial velocities towards the cluster mean. This is likely to happen if the stellar spectra are contaminated by nearby stars or the unresolved cluster light. As our approach to extract stellar spectra explicitly takes those contributions into account, it should be robust against such a bias. However, it is worth noting that McLaughlin et al. (2006) also found a bias in their sample of stars observed with a Fabry–Perot instrument, which in principle allows one to use a similar deblending approach as we did for the MUSE data (see Gebhardt et al. 1994). Yet another advantage of our approach is the usage of *HST* imaging that enables us to identify faint stars and blends that would not be resolved at seeing-limited resolution. The good agreement of our dynamical distance estimate with other available distance measurements makes us confident that our analysis is robust against the aforementioned bias.

The situation is less clear in NGC 6656 because the distance to this cluster is much less certain compared to NGC 104. The value in the Harris (1996) catalogue is based on Cudworth (1986) who measured a distance of 3.2 ± 0.3 kpc based on horizontal branch brightness and internal dynamics. Again, it could be that the existing radial velocity measurements lead to an underestimation of the true distance. In the near future, *Gaia* will hopefully settle this issue. The same is true for NGC 1851, where all three measurements of the dynamical distance are in agreement ($\sim$10.5 kpc) but are significantly below the value of 12.1 kpc determined by Walker (1998) from RR Lyrae stars.

6 DISCUSSION

Our analysis of the rotation fields in the previous section showed that the majority of the clusters in our sample show rotation. This finding is in agreement with previous studies that searched for rotation in globular clusters (e.g. Bellazzini et al. 2012; Fabricius et al. 2014). We now aim to investigate if the rotation signals show any correlations with other parameters of the sample clusters.

6.1 Is rotation related to ellipticity?

The work of Fabricius et al. (2014) revealed a correlation between the global ellipticity of a cluster and the strength of its central rotation. Interestingly though, neither Bellazzini et al. (2012) nor Lardo et al. (2015) found a correlation between rotation and ellipticity in their analyses. Under the assumption that globular clusters can be described by the same dynamical model, such as an isotropic oblate rotator, stronger rotation would be expected in more flattened systems. However, various effects can dilute a possible correlation, the most important ones being anisotropies, inclination effects or tidal forces from the Milky Way (see van den Bergh 2008, for an estimate of the impact of the latter).

To verify if our data suggest a link between rotation and ellipticity, we show in Fig. 11 the $\lambda_{\rm R,\,HL}$ values from Table 3 as a function of the ellipticities of the clusters. For those clusters where the radial coverage of the MUSE data ended before reaching the half-light radius $r_{\rm HL}$, we also included the results that would be obtained by scaling the original values by $r_{\rm HL}/r_{\rm max.}$ (open symbols in Fig. 11). This was done in light of the linear increase in $\lambda_{\rm R}$ that many clusters show for $r < r_{\rm HL}$ in Fig. 9.

The data shown in Fig. 11 suggest a trend of increasing rotation for more elliptical clusters. The statistical significance of a correlation is not high though, a Spearman rank test returns a probability of 3 per cent that the quantities are uncorrelated. If we use the extrapolated values instead for the clusters where we do not reach the half-light radius, this probability decreases to <1 per cent. We find a similarly strong correlation of ellipticity with the velocity gradient $\|\nabla v\|$. This can be verified in Table 4, where the results from the various Spearman correlation tests are summarized. Hence,

Downloaded from https://academic.oup.com/mnras/article-abstract/473/4/5591/4562634
by Liverpool John Moores University user
on 25 January 2018

Table 4. Results of the Spearman correlation tests between the properties of the rotation fields and various cluster parameters. (1) Primary parameter, taken from Table 3. (2) Secondary parameter: e – global photometric ellipticity, σ_0 – central velocity dispersion, $M_{V,t}$ – absolute cluster magnitude, [Fe/H] – metallicity, HB index – horizontal branch morphology, $\log t_h$ – logarithm of relaxation time at half-light radius in years. (3) Spearman correlation coefficient. The values in parentheses were obtained when extrapolating $\lambda_{R,HL}$ to the half-light radius for all clusters with $r_{max.}/r_{HL} < 1$ in Table 3. (4) Two-sided p-value. (5) Reference for secondary parameter: (a) this work; (b) Harris (1996); (c) Mackey & van den Bergh (2005); (d) Milone et al. (2017).

Par. 1 (1)	Par. 2 (2)	r_s (3)	p (4)	Ref. (5)
$\|\nabla v\|$	e	0.521	0.015	b
	σ_0	0.322	0.15	a
	$M_{V,t}$	−0.409	0.065	b
	[Fe/H]	−0.064	0.78	b
	HB index	0.092	0.7	c
	$\log t_h$	0.399	0.073	b
	N_1/N_{tot}	−0.549	0.022	d
$\lambda_{R,HL}$	e	0.475 (0.606)	0.03 (0.0036)	b
	σ_0	0.322 (0.257)	0.16 (0.26)	a
	$M_{V,t}$	−0.534 (−0.506)	0.013 (0.019)	b
	[Fe/H]	−0.154 (−0.151)	0.5 (0.51)	b
	HB index	0.014 (0.051)	0.95 (0.83)	c
	$\log t_h$	0.548 (0.642)	0.01 (0.0017)	b
	N_1/N_{tot}	−0.531 (−0.488)	0.028 (0.047)	d

our results seem to confirm the finding of Fabricius et al. (2014) that more elliptical clusters show stronger rotation, albeit with low significance.

Also shown in Fig. 11 is the predicted behaviour of an isotropic oblate rotator, using the formulae from Cappellari et al. (2007) and Emsellem et al. (2007). Most of our targets lie significantly below the expectation for an isotropic oblate rotator seen edge-on. As inclination effects play a minor role in the isotropic case (see dotted lines in Fig. 11), mild anisotropies could provide an explanation for the excess in ellipticity at a given value of λ_R (see the model curves for anisotropies of $\beta = 0.1$ and 0.2). While Watkins et al. (2015a) found that the anisotropies in the centres of most clusters are small, they might be more important in the outskirts of the clusters where the ellipticities were measured (e.g. Giersz & Heggie 1997; Tiongco, Vesperini & Varri 2016; Zocchi et al. 2016).

Another result that lead Fabricius et al. (2014) to conclude that there is a link between rotation and flattening of the clusters was that for most of their targets, the kinematic angles and the position angles of the photometric semi-major axes agreed within their relative uncertainties. To check if this is also true for our sample, we performed the same analysis as Fabricius et al. (2014) and determined photometric position angles from a principal component analysis of the available photometry. As in Section 5.3, we applied a magnitude cut to the photometric catalogues to avoid biases due to incompleteness and only considered radii <80 arcsec where the catalogues covered the full circle. The photometric position angles are compared to our measurements of the rotation axis angles in Figs 5 and A1. In the case of isotropic oblate rotators, one would expect both angles to be separated by 90°. This is indeed the case for the vast majority of the rotating clusters in our sample. A notable exception is NGC 5139, where the axes seem to be aligned. This might indicate that in NGC 5139 the central kinematics are more complex than in the remaining clusters of our sample, which is also suggested by the detection of (mild) radial anisotropy around its centre (van de Ven et al. 2006; van der Marel & Anderson 2010). Such complex kinematics are observed in early-type galaxies, including dwarf spheroidals (e.g. Ebrová & Łokas 2015; Kacharov et al. 2017) and massive ellipticals (e.g. Tsatsi et al. 2017; Krajnović et al., in preparation[6]), and are commonly explained by invoking mergers – a possibility that is also often used to explain the peculiar chemistry of NGC 5139 (see Section 6.3 below).

6.2 Rotation and globular cluster formation

Several correlations between the rotation of a cluster and other fundamental properties are discussed in the literature. Bellazzini et al. (2012) and Lardo et al. (2015, who added a few additional clusters to the sample of Bellazzini et al. 2012) report increasing rotation velocities v_{rot} for more metal-rich clusters and clusters with redder horizontal branches, where the colour of the horizontal branch was quantified using the HB index as given by Lee (1990) or Mackey & van den Bergh (2005). However, no correlation with metallicity was found by Kimmig et al. (2015) and also our data do not confirm these results. As can be verified from the central panel of Fig. 12 and the values in Table 4, no correlations exist in our sample with the cluster metallicities or the morphologies of their horizontal branches. The latter is surprising as the correlation between rotation velocity and horizontal branch morphology is the most significant one in the data set of Bellazzini et al. (2012). When comparing our rotation results with those of Bellazzini et al. (2012), it is striking that the largest discrepancies are observed for NGC 6388 and NGC 6441, the most metal-rich clusters of our sample, for which we obtain a much weaker rotation signal. As the horizontal branch morphology is linked to the metallicity (e.g. Lee 1990), this may partly explain why we do not see a correlation with either quantity in our data. Again, we emphasize the different radial regimes probed by our study and by Bellazzini et al. (2012).

Bellazzini et al. (2012) also find v_{rot} to correlate with the luminosity and the central velocity dispersion of a cluster. The latter is in agreement with the correlation between the velocity gradient $\|\nabla v\|$ and the velocity dispersion reported by Fabricius et al. (2014), who speculated that undetected rotation had spuriously increased the velocity dispersion measurements in the literature. As the velocity dispersions obtained in this work are robust against such biases, we are able to test this hypothesis. We find only a mild correlation between either $\lambda_{R,HL}$ or $\|\nabla v\|$ and the updated values of the velocity dispersion, with false-alarm probabilities of around 15 per cent (see Fig. 12 and Table 4). Yet our study confirms that the rotational support increases with the luminosity of a cluster (expressed as an anti-correlation between $\lambda_{R,HL}$ and the absolute magnitude $M_{V,t}$ of a cluster in Table 4). Under the assumption that globular clusters have comparable mass-to-light ratios (e.g. Baumgardt 2017), this would imply that the rotational support increases in more massive clusters. The correlation with velocity dispersion might be secondary then, because more massive clusters tend to have higher velocity dispersions.

As can be seen in the right-hand panel of Fig. 12 and verified in Table 4, in our sample the relaxation time at the half-light radius, t_h (taken from Harris 1996), shows the strongest correlation with $\lambda_{R,HL}$, especially when using the extrapolated values for the clusters

[6] see http://www.eso.org/sci/meetings/2015/StellarHalos2015/talks_presentation/emsellem_M3G.pdf

Downloaded from https://academic.oup.com/mnras/article-abstract/473/4/5591/4562634
by Liverpool John Moores University user
on 25 January 2018

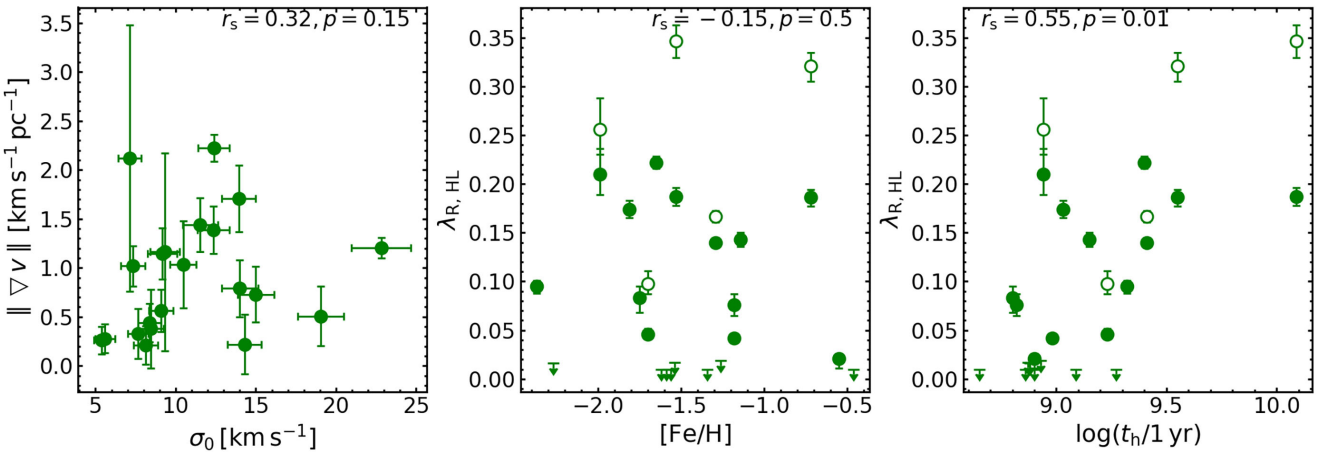

Figure 12. Relations between rotation strengths and various fundamental properties of the clusters discussed in the text, namely the central velocity dispersion σ_0 (left), the metallicity [Fe/H] (middle) and the logarithm of the relaxation time at the half-light radius $\log t_h$ (right). As in Fig. 11, we show the extrapolated values of $\lambda_{R,HL}$ as open symbols for clusters without coverage of the half-light radii. To the top of each panel, we provide the Spearman correlation coefficient and the two-sided p-value of the correlation. For the origin of the various cluster properties, see Table 4.

without coverage of the half-light radius.[7] This is not completely unexpected, as angular momentum is transported outwards by relaxation processes. Hence, our data support a scenario in which the globular cluster inherited angular momentum from the collapsing molecular cloud that would then be slowly dissipated away by two-body relaxation. Indeed, recent theoretical studies (Lee & Hennebelle 2016; Mapelli 2017) suggest that massive star clusters are born with significant amounts of rotation. In addition, rotation is found in both intermediate-age (Davies et al. 2011; Mackey et al. 2013) and young massive (Hénault-Brunet et al. 2012) clusters, supporting such a scenario. In the future, systematic studies of the rotation properties as a function of cluster age will be crucial to make further progress in this direction.

The aforementioned scenario might also explain the discrepancies we observe in comparison to the study of Bellazzini et al. (2012). Whereas our data focus on the central cluster regions where dissipation dominates because of the short relaxation times, Bellazzini et al. (2012) probe the outskirts of the clusters where rotation patterns imprinted during the formation of the cluster would be longer lived and hence possible differences connected to the metal content of the molecular cloud are still observable.

In view of the dissipation of angular momentum, it is interesting to look at the core-collapsed clusters of our sample. However, no clear picture emerges. While NCG 6522, NGC 6681 and NGC 7099 are indeed among the least rotating clusters of our sample, rather strong rotation fields are observed in NGC 7078 and possibly also NGC 6293. Therefore, it remains unclear how strongly the central rotation is affected by core collapse.

In light of the evidence for a decoupled core in NGC 7078 (van den Bosch et al. 2006), we also checked whether any other cluster from our sample shows a similar rotation behaviour (enhanced rotation in combination with a change in position angle) in its centre. We observe similar features in our data of NGC 362, NGC 5904, NGC 6254 and NGC 6266, suggesting that this feature is not unique to NGC 7078. Two of the four clusters (NGC 362 and NGC 6266) are labelled as possible core-collapsed clusters in Harris (1996), so the feature does not seem to be specific to core-collapsed clusters. However, dedicated modelling will be needed to investigate this further.

[7] We sound a note of caution that the calculation of the relaxation times included the same half-light radii r_{HL} (see formulae in Djorgovski 1993) we used as a reference to measure λ_R, cf. Section 5.3. However, no correlation exists between λ_R and r_{rHL} itself in our data.

6.3 Rotation and multiple populations

Finally, we briefly discuss our findings with regard to the open issue of the origin of multiple populations inside the clusters. Several authors discussed the possibility of finding dynamical signatures stemming from one or the other formation scenario. Gavagnin, Mapelli & Lake (2016) investigated the possibility that iron-complex globular clusters were created from mergers in dwarf galaxies and argued that in this case, the clusters should be rotating and flattened. Our sample includes several clusters with reported spreads in heavy elements, namely NGC 1851 (Yong & Grundahl 2008), NGC 5139 (e.g. Norris & Da Costa 1995), NGC 6656 (Marino et al. 2009, but also see Mucciarelli et al. 2015) and NGC 7089 (Lardo et al. 2013). We note that all of those clusters show a clear rotation signal in our data but no clear distinction can be made with respect to the 'normal' clusters. Gavagnin et al. (2016) predict that in merger remnants, the rotation velocity should increase out to about the half-light radius and stay approximately constant beyond it. The increase at small distances to the centre is also visible in our data. Beyond the half-light radius, we lack the data for a detailed comparison. However, in NGC 1851, we see evidence that the rotation velocity decreases again.

For a follow-up study, we plan to investigate if the various populations inside the clusters show different rotation patterns. According to the simulations of Hénault-Brunet et al. (2015), a second population forming from the ejecta of a primordial one should rotate faster than the latter while the opposite should be true in the early disc accretion scenario proposed by Bastian et al. (2013). While the chances of still finding such differences are higher beyond the half-light radius (because of the longer relaxation times), the detection of clear rotation fields even around the cluster centres might indicate that differences are still observable within the MUSE footprints. A first step into the direction of studying chemically resolved rotation properties has been done by Cordero et al. (2017) who found the extreme population of NGC 6205 to have a higher rotation rate than the other two populations (although the sample sizes per population were still small).

Mastrobuono-Battisti & Perets (2016) also studied the evolution of a rotating disc of second-population stars in globular clusters.

Downloaded from https://academic.oup.com/mnras/article-abstract/473/4/5591/4562634
by Liverpool John Moores University user
on 25 January 2018

According to their simulations, a positive correlation would be expected between the cluster ellipticities and the relaxation times. Indeed, in our sample, such a correlation is observed – which is not very surprising as both quantities correlate with the strength of the cluster rotation. Mastrobuono-Battisti & Perets (2016) further speculate about a correlation between ellipticity and the fraction of second-population stars. When we use the fractions of first-population stars reported by Milone et al. (2017) at face value, we indeed see some evidence for an anti-correlation (cf. Table 4), which would support such a scenario. But this finding may just be a consequence of the increase of rotation with cluster mass that we observe as Milone et al. (2017) find the fraction of second-population stars to also increase with cluster mass. In a forthcoming publication, we plan to investigate possible relations between rotation and multiple populations in more detail.

7 CONCLUSIONS

We presented the first results from our MUSE survey of 25 Galactic globular clusters and showed that the data are well suited to investigate the central dynamics of the clusters in the sample. In comparison to previous radial velocity samples, a big advantage of our approach is a complete coverage of the cluster centres, out to approximately the half-light radii of our targets. In combination with a data analysis that accounts for stellar blends, this enables us to obtain average sample sizes of currently around 9000 stars per cluster. Our data sets represent the largest spectroscopic samples that have been obtained so far for the vast majority of our targets.

Despite the limited spectral resolution of MUSE and the complexity of the instrument (which analyses the light using 24 spectrographs), we are able to achieve a velocity accuracy of 1–2 km s^{-1}, well below the velocity dispersions of the clusters in our sample. The uncertainties for the individual stellar velocities will be higher depending on the S/N of the extracted spectra, of course. However, reliable velocity measurements are still possible at S/N $\sim$ 5–10.

We constructed two-dimensional maps as well as radial profiles of the average velocities and velocity dispersions for each cluster. They show that the majority of our sample rotates in the central cluster regions. Our finding that the amount of rotation correlates with the ellipticities of a cluster confirms the results by Fabricius et al. (2014) that central rotation affects the overall appearance of a cluster. Further, we find a clear correlation between the rotation strengths and the relaxation times at the half-light radii. This finding supports a scenario in which the clusters are born with a significant amount of angular momentum that is dissipated over their lifetimes as a result of two-body relaxation.

The velocity dispersion profiles show a good agreement with profiles available in the literature (with the exception of NGC 6121 and possibly NGC 3201) but reach closer to the cluster centres in most cases. By means of a comparison with the proper motion data of Watkins et al. (2015a), we derived dynamical distances for 14 clusters. They are usually in good agreement with previous estimates, albeit a few exceptions are found again. For NGC 104, our updated value for the dynamical distance is in better agreement with other distance estimates, suggesting that the existing radial velocity data near the cluster centre underestimated the true velocity dispersion.

ACKNOWLEDGEMENTS

We thank the anonymous referee for a careful reading of our manuscript and for providing us with a report that contained many good suggestions to further improve the paper. We also thank Nate Bastian and the members of the MUSE consortium not listed among the co-authors for inspiring discussions and support during stages of this work. SK, SD and PMW acknowledge support from the German Ministry for Education and Science (BMBF Verbundforschung) through project MUSE-AO, grants 05A14BAC, 05A14MGA and 05A17MGA. SK and SD also acknowledge support from the German Research Foundation (DFG) through projects KA 4537/2-1 and DR 281/35-1. Based on observations made with ESO Telescopes at the La Silla Paranal Observatory under programme IDs 094.D-0142, 095.D-0629, 096.D-0175 and 097.D-0295. Also based on observations made with the NASA/ESA *Hubble Space Telescope*, obtained from the data archive at the Space Telescope Science Institute. STScI is operated by the Association of Universities for Research in Astronomy, Inc. under NASA contract NAS 5-26555. This research made use of ASTROPY, a community-developed core PYTHON package for Astronomy (Astropy Collaboration 2013).

REFERENCES

Aarseth S. J., Henon M., Wielen R., 1974, A&A, 37, 183
Anderson J. et al., 2008, AJ, 135, 2055
Astropy Collaboration et al., 2013, A&A, 558, A33
Bacon R. et al., 2010, Proc. SPIE, 7735, 773508
Bastian N., 2015, preprint (arXiv:1510.01330)
Bastian N., Lamers H. J. G. L. M., de Mink S. E., Longmore S. N., Goodwin S. P., Gieles M., 2013, MNRAS, 436, 2398
Baumgardt H., 2017, MNRAS, 464, 2174
Baumgardt H., Makino J., 2003, MNRAS, 340, 227
Bellazzini M., Bragaglia A., Carretta E., Gratton R. G., Lucatello S., Catanzaro G., Leone F., 2012, A&A, 538, A18
Bellini A. et al., 2014, ApJ, 797, 115
Bellini A. et al., 2015, ApJ, 810, L13
Bellini A., Bianchini P., Varri A. L., Anderson J., Piotto G., van der Marel R. P., Vesperini E., Watkins L. L., 2017, ApJ, 844, 167
Bertin E., Mellier Y., Radovich M., Missonnier G., Didelon P., Morin B., 2002, in Bohlender D. A., Durand D., Handley T. H., eds, ASP Conf. Ser. Vol. 281, Astronomical Data Analysis Software and Systems XI. Astron. Soc. Pac., San Francisco, p. 228
Bianchini P., Varri A. L., Bertin G., Zocchi A., 2013, ApJ, 772, 67
Bianchini P., van de Ven G., Norris M. A., Schinnerer E., Varri A. L., 2016, MNRAS, 458, 3644
Binney J., 2005, MNRAS, 363, 937
Boberg O. M., Vesperini E., Friel E. D., Tiongco M. A., Varri A. L., 2017, ApJ, 841, 114
Bogdanov S., Heinke C. O., Özel F., Güver T., 2016, ApJ, 831, 184
Bressan A., Marigo P., Girardi L., Salasnich B., Dal Cero C., Rubele S., Nanni A., 2012, MNRAS, 427, 127
Cappellari M., Copin Y., 2003, MNRAS, 342, 345
Cappellari M. et al., 2007, MNRAS, 379, 418
Carretta E. et al., 2009, A&A, 505, 117
Chomiuk L., Strader J., Maccarone T. J., Miller-Jones J. C. A., Heinke C., Noyola E., Seth A. C., Ransom S., 2013, ApJ, 777, 69
Copin Y. et al., 2001, in Combes F., Barret D., Thévenin F., eds, SF2A-2001: Semaine de l'Astrophysique Francaise. p. 289
Cordero M. J., Hénault-Brunet V., Pilachowski C. A., Balbinot E., Johnson C. I., Varri A. L., 2017, MNRAS, 465, 3515
Cote P., Welch D. L., Fischer P., Gebhardt K., 1995, ApJ, 454, 788
Cottaar M., Hénault-Brunet V., 2014, A&A, 562, A20
Cottaar M., Meyer M. R., Parker R. J., 2012, A&A, 547, A35
Cudworth K. M., 1986, AJ, 92, 348
Da Costa G. S., Freeman K. C., 1976, ApJ, 206, 128
Davies B., Bastian N., Gieles M., Seth A. C., Mengel S., Konstantopoulos I. S., 2011, MNRAS, 411, 1386
Djorgovski S., 1993, in Djorgovski S. G., Meylan G., eds, ASP Conf. Ser. Vol. 50, Structure and Dynamics of Globular Clusters. Astron. Soc. Pac., San Francisco, p. 373

Downloaded from https://academic.oup.com/mnras/article-abstract/473/4/5591/4562634
by Liverpool John Moores University user
on 25 January 2018

Dolphin A. E., 2000, PASP, 112, 1383
Ebrová I., Łokas E. L., 2015, ApJ, 813, 10
Emsellem E. et al., 2007, MNRAS, 379, 401
Fabricius M. H. et al., 2014, ApJ, 787, L26
Fiestas J., Spurzem R., Kim E., 2006, MNRAS, 373, 677
Foreman-Mackey D., Hogg D. W., Lang D., Goodman J., 2013, PASP, 125, 306
Gavagnin E., Mapelli M., Lake G., 2016, MNRAS, 461, 1276
Gebhardt K., Pryor C., Williams T. B., Hesser J. E., 1994, AJ, 107, 2067
Geller A. M. et al., 2017, ApJ, 840, 66
Gieles M., Zocchi A., 2015, MNRAS, 454, 576
Giersz M., Heggie D. C., 1997, MNRAS, 286, 709
Giersz M., Heggie D. C., Hurley J. R., Hypki A., 2013, MNRAS, 431, 2184
Gunn J. E., Griffin R. F., 1979, AJ, 84, 752
Harris W. E., 1996, AJ, 112, 1487
Hénault-Brunet V. et al., 2012, A&A, 545, L1
Hénault-Brunet V., Gieles M., Agertz O., Read J. I., 2015, MNRAS, 450, 1164
Husser T.-O., Wende-von Berg S., Dreizler S., Homeier D., Reiners A., Barman T., Hauschildt P. H., 2013, A&A, 553, A6
Husser T.-O. et al., 2016, A&A, 588, A148 (Paper I)
Jeffreson S. M. R. et al., 2017, MNRAS, 469, 4740
Jesseit R., Cappellari M., Naab T., Emsellem E., Burkert A., 2009, MNRAS, 397, 1202
Kacharov N. et al., 2014, A&A, 567, A69
Kacharov N. et al., 2017, MNRAS, 466, 2006
Kamann S., Wisotzki L., Roth M. M., 2013, A&A, 549, A71
Kamann S., Wisotzki L., Roth M. M., Gerssen J., Husser T.-O., Sandin C., Weilbacher P., 2014, A&A, 566, A58
Kamann S. et al., 2016, A&A, 588, A149 (Paper II)
Kiminki D. C., Kobulnicky H. A., 2012, ApJ, 751, 4
Kimmig B., Seth A., Ivans I. I., Strader J., Caldwell N., Anderton T., Gregersen D., 2015, AJ, 149, 53
King I. R., 1966, AJ, 71, 64
Krajnović D., Cappellari M., Emsellem E., McDermid R. M., de Zeeuw P. T., 2005, MNRAS, 357, 1113
Krajnović D., Cappellari M., de Zeeuw P. T., Copin Y., 2006, MNRAS, 366, 787
Lagoute C., Longaretti P.-Y., 1996, A&A, 308, 441
Lane R. R. et al., 2010, MNRAS, 406, 2732
Lane R. R., Kiss L. L., Lewis G. F., Ibata R. A., Siebert A., Bedding T. R., Székely P., Szabó G. M., 2011, A&A, 530, A31
Lanzoni B. et al., 2013, ApJ, 769, 107
Lapenna E., Origlia L., Mucciarelli A., Lanzoni B., Ferraro F. R., Dalessandro E., Valenti E., Cirasuolo M., 2015, ApJ, 798, 23
Lardo C. et al., 2013, MNRAS, 433, 1941
Lardo C. et al., 2015, A&A, 573, A115
Lee Y.-W., 1990, ApJ, 363, 159
Lee Y.-N., Hennebelle P., 2016, A&A, 591, A30
Lützgendorf N., Kissler-Patig M., Noyola E., Jalali B., de Zeeuw P. T., Gebhardt K., Baumgardt H., 2011, A&A, 533, A36
Lützgendorf N. et al., 2013, A&A, 552, A49
Mackey A. D., van den Bergh S., 2005, MNRAS, 360, 631
Mackey A. D., Da Costa G. S., Ferguson A. M. N., Yong D., 2013, ApJ, 762, 65
McLaughlin D. E., van der Marel R. P., 2005, ApJS, 161, 304
McLaughlin D. E., Anderson J., Meylan G., Gebhardt K., Pryor C., Minniti D., Phinney S., 2006, ApJS, 166, 249
Mapelli M., 2017, MNRAS, 467, 3255
Marino A. F., Milone A. P., Piotto G., Villanova S., Bedin L. R., Bellini A., Renzini A., 2009, A&A, 505, 1099
Mastrobuono-Battisti A., Perets H. B., 2016, ApJ, 823, 61
Mathieu R. D., van den Berg M., Torres G., Latham D., Verbunt F., Stassun K., 2003, AJ, 125, 246
Merritt D., Meylan G., Mayor M., 1997, AJ, 114, 1074
Meylan G., Mayor M., 1986, A&A, 166, 122
Michie R. W., 1963, MNRAS, 125, 127
Milone A. P. et al., 2012, A&A, 540, A16
Milone A. P. et al., 2017, MNRAS, 464, 3636
Mucciarelli A., Lapenna E., Massari D., Pancino E., Stetson P. B., Ferraro F. R., Lanzoni B., Lardo C., 2015, ApJ, 809, 128
Norris J. E., Da Costa G. S., 1995, ApJ, 447, 680
Noyola E., Gebhardt K., 2006, AJ, 132, 447
Noyola E., Gebhardt K., Bergmann M., 2008, ApJ, 676, 1008
Pancino E., Bellazzini M., Giuffrida G., Marinoni S., 2017, MNRAS, 467, 412
Peuten M., Zocchi A., Gieles M., Gualandris A., Hénault-Brunet V., 2016, MNRAS, 462, 2333
Piotto G. et al., 2002, A&A, 391, 945
Pryor C., Meylan G., 1993, in Djorgovski S. G., Meylan G., eds, ASP Conf. Ser. Vol. 50, Structure and Dynamics of Globular Clusters. Astron. Soc. Pac., San Francisco, p. 357
Pryor C. P., Latham D. W., Hazen M. L., 1988, AJ, 96, 123
Renzini A. et al., 2015, MNRAS, 454, 4197
Richer H. B., Heyl J., Anderson J., Kalirai J. S., Shara M. M., Dotter A., Fahlman G. G., Rich R. M., 2013, ApJ, 771, L15
Robin A. C., Reylé C., Derrière S., Picaud S., 2003, A&A, 409, 523
Rodriguez C. L., Morscher M., Wang L., Chatterjee S., Rasio F. A., Spurzem R., 2016, MNRAS, 463, 2109
Sarajedini A. et al., 2007, AJ, 133, 1658
Sollima A., Bellazzini M., Smart R. L., Correnti M., Pancino E., Ferraro F. R., Romano D., 2009, MNRAS, 396, 2183
Sollima A., Dalessandro E., Beccari G., Pallanca C., 2017, MNRAS, 464, 3871
Sommariva V., Piotto G., Rejkuba M., Bedin L. R., Heggie D. C., Milone A., Mathieu R. D., Moretti A., 2008, in Vesperini E., Giersz M., Sills A., eds, Proc. IAU Symp. 246, Dynamical Evolution of Dense Stellar Systems. Cambridge Univ. Press, Cambridge, p. 277
Stoehr F. et al., 2008, in Argyle R. W., Bunclark P. S., Lewis J. R., eds, ASP Conf. Ser. Vol. 394, Astronomical Data Analysis Software and Systems XVII. Astron. Soc. Pac., San Francisco, p. 505
Tiongco M. A., Vesperini E., Varri A. L., 2016, MNRAS, 455, 3693
Tonry J., Davis M., 1979, AJ, 84, 1511
Trager S. C., King I. R., Djorgovski S., 1995, AJ, 109, 218
Tsatsi A., Lyubenova M., van de Ven G., Chang J., Aguerri J. A. L., Falcón-Barroso J., Macciò A. V., 2017, A&A, 606, A62
van de Ven G., van den Bosch R. C. E., Verolme E. K., de Zeeuw P. T., 2006, A&A, 445, 513
van den Bergh S., 2008, AJ, 135, 1731
van den Bosch R., de Zeeuw T., Gebhardt K., Noyola E., van de Ven G., 2006, ApJ, 641, 852
van der Marel R. P., Anderson J., 2010, ApJ, 710, 1063
van der Marel R. P., Franx M., 1993, ApJ, 407, 525
Varri A. L., Bertin G., 2012, A&A, 540, A94
Vriend W.-J., 2015, in Science Operations 2015: Science Data Management – An ESO/ESA Workshop. p. 1, Available at https://www.eso.org/sci/meetings/2015/SciOps2015.html
Walker A. R., 1998, AJ, 116, 220
Walker M. G., Mateo M., Olszewski E. W., Sen B., Woodroofe M., 2009, AJ, 137, 3109
Wang L. et al., 2016, MNRAS, 458, 1450
Watkins L. L., van der Marel R. P., Bellini A., Anderson J., 2015a, ApJ, 803, 29
Watkins L. L., van der Marel R. P., Bellini A., Anderson J., 2015b, ApJ, 812, 149
Weilbacher P. M., Streicher O., Urrutia T., Jarno A., Pécontal-Rousset A., Bacon R., Böhm P., 2012, Proc. SIPE, 8451, 84510B
Weilbacher P. M., Streicher O., Urrutia T., Pécontal-Rousset A., Jarno A., Bacon R., 2014, in Manset N., Forshay P., eds, ASP Conf. Ser. Vol. 485, Astronomical Data Analysis Software and Systems XXIII. Astron. Soc. Pac., San Francisco, p. 451
Wendt M. et al., 2017, A&A, preprint (arXiv:1709.03982)
Woodley K. A. et al., 2012, AJ, 143, 50
Yong D., Grundahl F., 2008, ApJ, 672, L29

Downloaded from https://academic.oup.com/mnras/article-abstract/473/4/5591/4562634
by Liverpool John Moores University user
on 25 January 2018

Zocchi A., Gieles M., Hénault-Brunet V., Varri A. L., 2016, MNRAS, 462, 696
Zocchi A., Gieles M., Hénault-Brunet V., 2017, MNRAS, 468, 4429

APPENDIX A: KINEMATICS PLOTS FOR REMAINING CLUSTERS

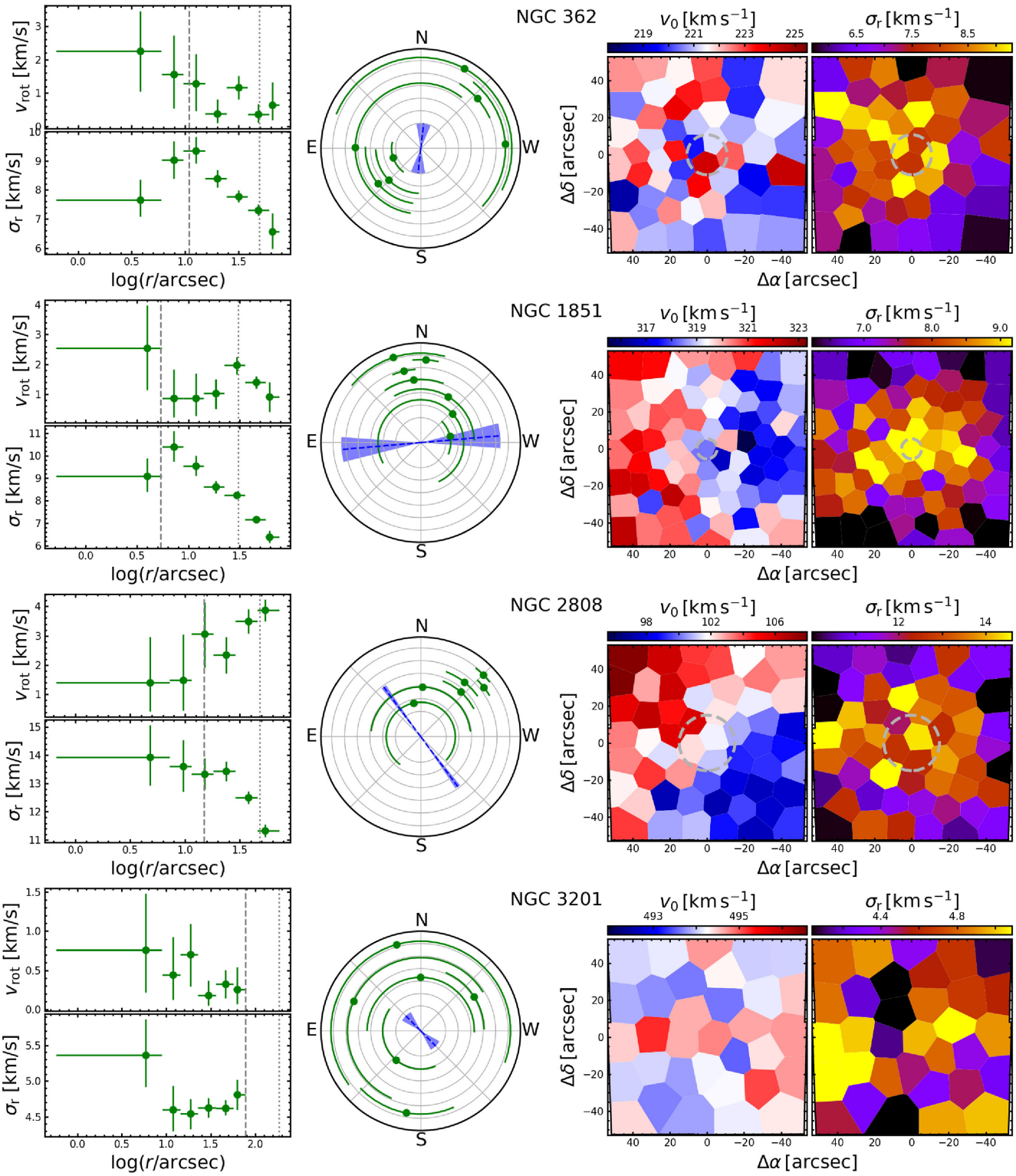

Figure A1. As Fig. 5 but for NGC 362, NGC 1851, NGC 2808, NGC 3201, NGC 5139, NGC 5904, NGC 6093, NGC 6121, NGC 6254, NGC 6266, NGC 6293, NGC 6388, NGC 6522, NGC 6541, NGC 6656, NGC 6681, NGC 6752, NGC 7078 and NGC 7099.

Downloaded from https://academic.oup.com/mnras/article-abstract/473/4/5591/4562634
by Liverpool John Moores University user
on 25 January 2018

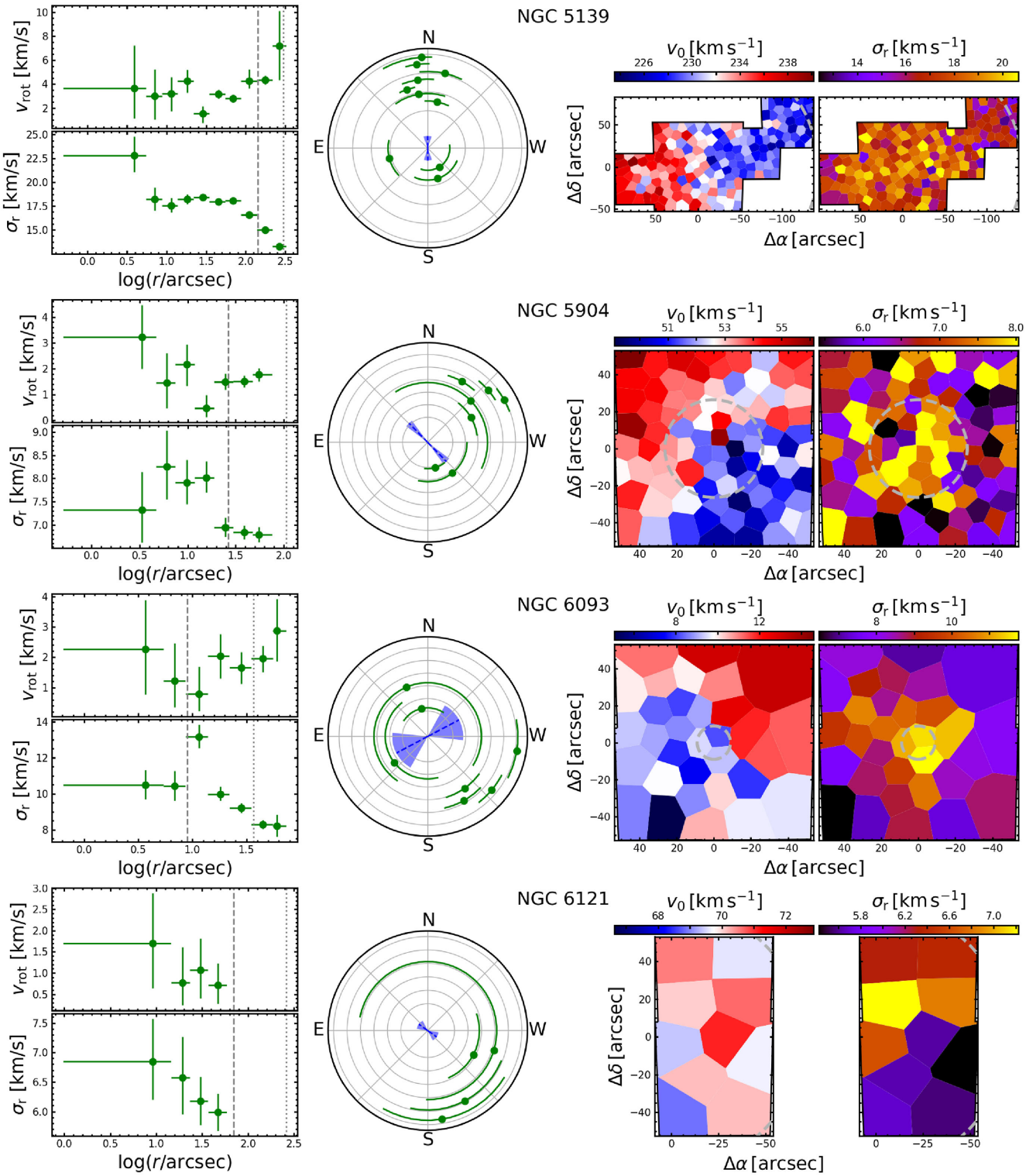

Figure A1 – *continued*

Downloaded from https://academic.oup.com/mnras/article-abstract/473/4/5591/4562634
by Liverpool John Moores University user
on 25 January 2018

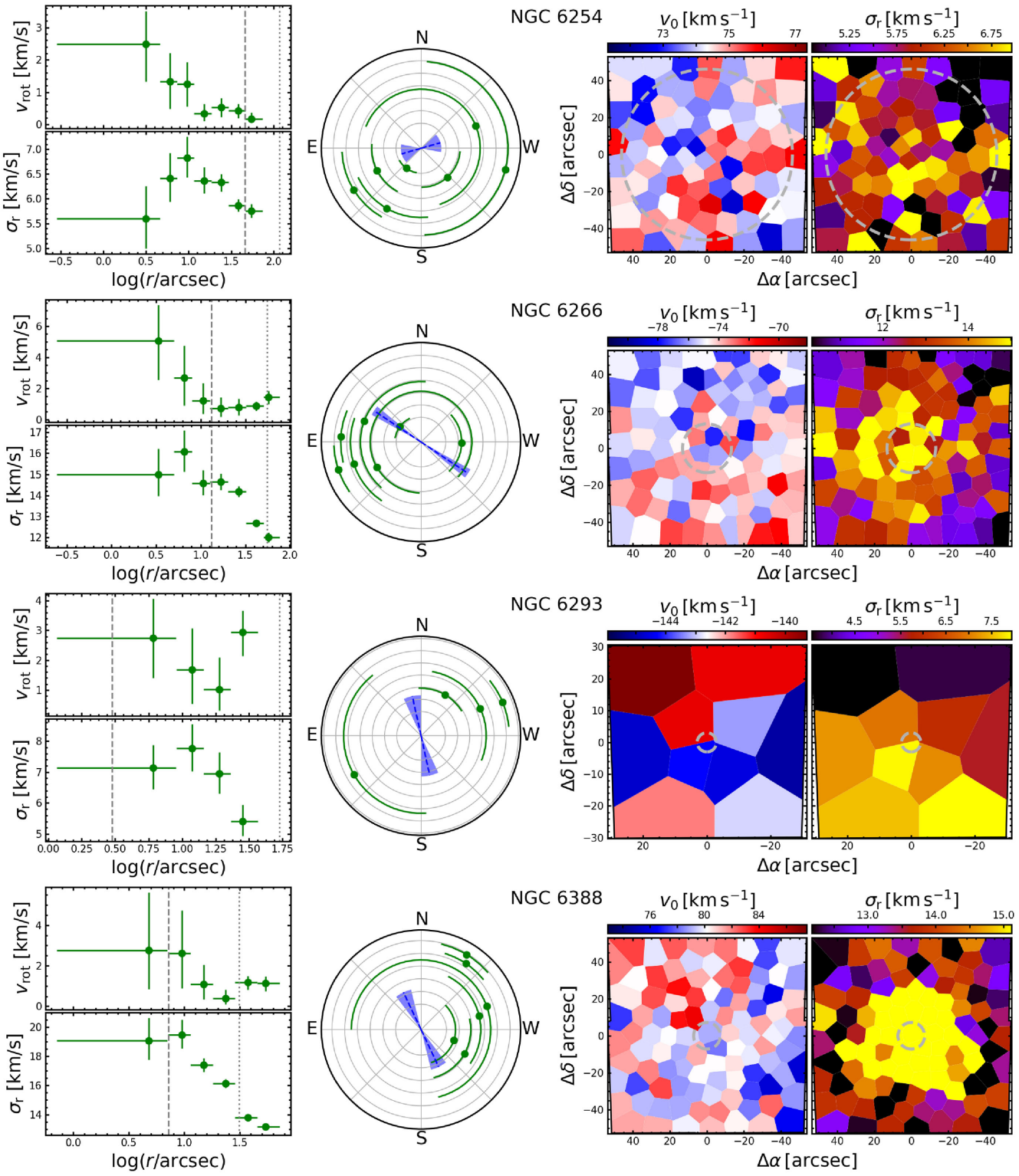

Figure A1 – *continued*

Downloaded from https://academic.oup.com/mnras/article-abstract/473/4/5591/4562634
by Liverpool John Moores University user
on 25 January 2018

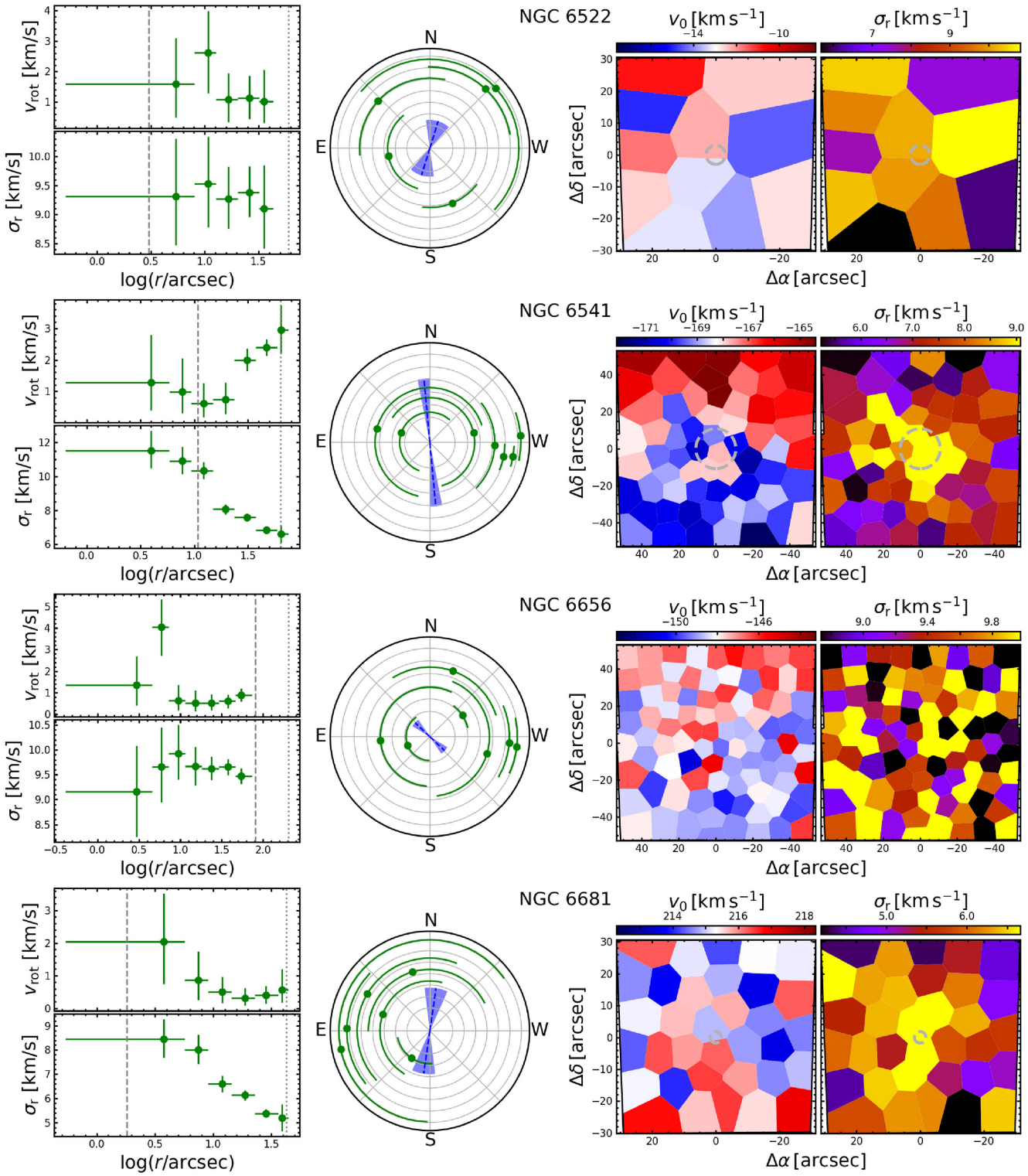

Figure A1 – *continued*

Downloaded from https://academic.oup.com/mnras/article-abstract/473/4/5591/4562634
by Liverpool John Moores University user
on 25 January 2018

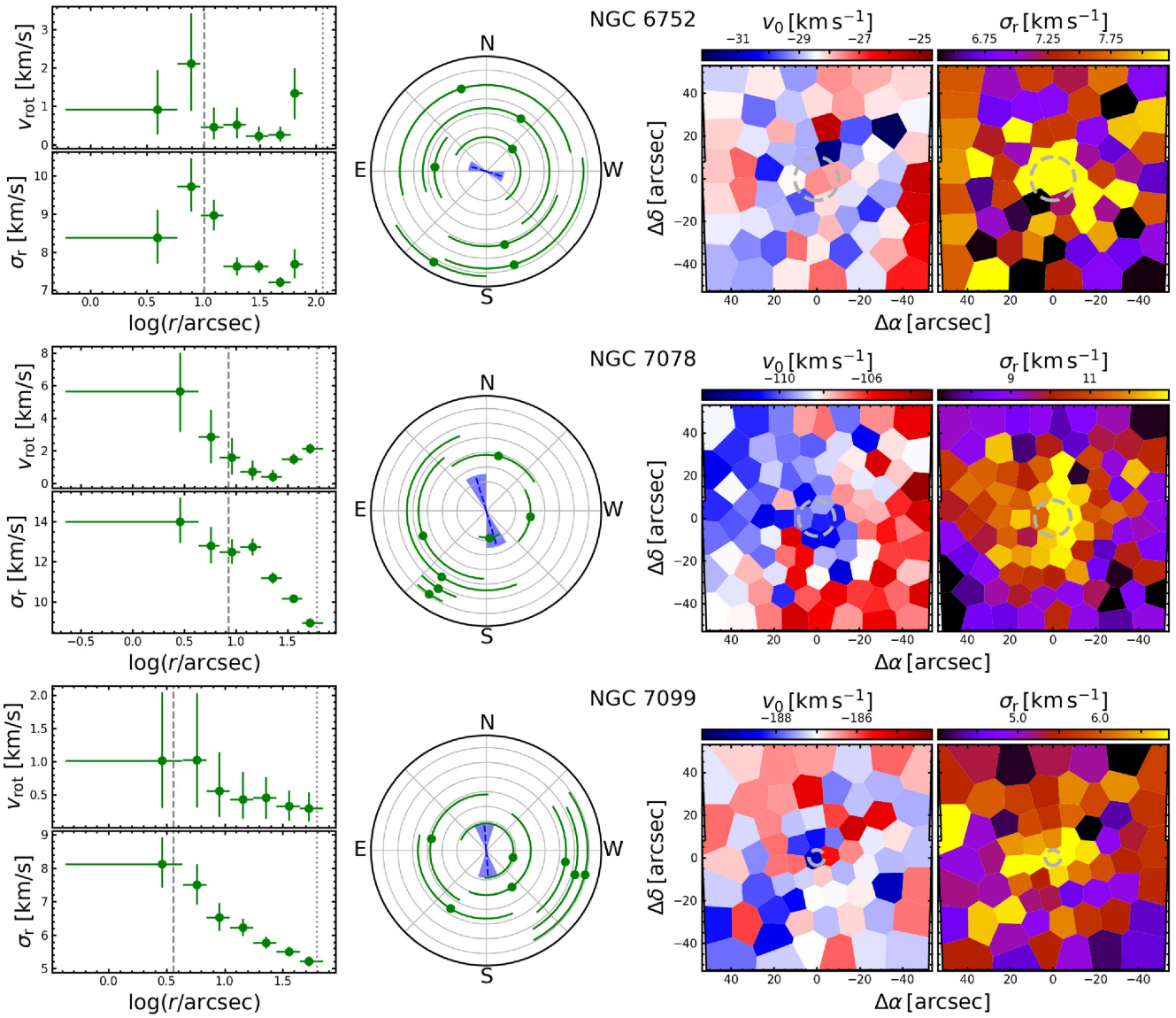

Figure A1 – *continued*

Downloaded from https://academic.oup.com/mnras/article-abstract/473/4/5591/4562634
by Liverpool John Moores University user
on 25 January 2018

APPENDIX B: RADIAL PROFILE DATA

Table B1. Radial profiles of the cluster dynamics from the MUSE sample. For each bin, r indicates the mean distance of the stars to the cluster centre while the associated uncertainties give its full radial extent. Otherwise, we provide the median and the 16th and 84th percentiles of the parameter distributions obtained from the MCMC chains. The effective masses were determined as outlined in Section 5.2.

NGC	r (arcsec)	θ_0 (rad)	$v_{\rm rot}$ (km s^{-1})	$\sigma_{\rm r}$ (km s^{-1})	$M_{\rm eff.}$ ($M_\odot$)
104	$4.2^{+2.4}_{-3.8}$	$2.63^{+0.85}_{-0.97}$	$2.18^{+1.77}_{-1.43}$	$12.37^{+1.05}_{-0.89}$	0.81
104	$8.9^{+1.6}_{-2.3}$	$2.88^{+0.53}_{-0.48}$	$3.50^{+1.69}_{-1.72}$	$13.10^{+0.96}_{-0.81}$	0.81
104	$13.6^{+3.0}_{-3.2}$	$2.07^{+1.08}_{-1.25}$	$0.96^{+0.91}_{-0.68}$	$12.29^{+0.53}_{-0.51}$	0.81
104	$21.9^{+4.4}_{-5.3}$	$2.58^{+0.46}_{-0.51}$	$1.29^{+0.60}_{-0.66}$	$12.23^{+0.31}_{-0.31}$	0.81
104	$34.7^{+7.0}_{-8.4}$	$2.26^{+0.15}_{-0.14}$	$2.35^{+0.36}_{-0.35}$	$12.02^{+0.18}_{-0.18}$	0.81
104	$53.6^{+12.6}_{-11.8}$	$2.25^{+0.07}_{-0.08}$	$3.22^{+0.24}_{-0.24}$	$11.41^{+0.13}_{-0.13}$	0.80
104	$85.1^{+19.8}_{-18.9}$	$2.49^{+0.09}_{-0.10}$	$3.94^{+0.29}_{-0.26}$	$11.30^{+0.12}_{-0.11}$	0.75
104	$114.4^{+24.4}_{-9.5}$	$2.36^{+0.36}_{-0.44}$	$4.03^{+0.70}_{-0.41}$	$10.54^{+0.20}_{-0.20}$	0.72
362	$3.8^{+2.2}_{-3.2}$	$1.90^{+0.59}_{-0.52}$	$2.26^{+1.18}_{-1.21}$	$7.66^{+0.69}_{-0.58}$	0.81
362	$7.8^{+1.8}_{-1.8}$	$2.35^{+0.73}_{-0.74}$	$1.56^{+1.16}_{-1.02}$	$9.03^{+0.66}_{-0.64}$	0.81
362	$12.6^{+2.6}_{-3.0}$	$2.26^{+0.73}_{-0.70}$	$1.29^{+0.88}_{-0.81}$	$9.34^{+0.48}_{-0.43}$	0.81
362	$20.0^{+4.2}_{-4.8}$	$1.55^{+1.42}_{-2.22}$	$0.39^{+0.44}_{-0.28}$	$8.39^{+0.30}_{-0.29}$	0.81
362	$31.6^{+6.7}_{-7.5}$	$-0.85^{+0.30}_{-0.30}$	$1.16^{+0.35}_{-0.35}$	$7.77^{+0.21}_{-0.21}$	0.80
362	$48.0^{+12.8}_{-9.6}$	$-1.52^{+0.84}_{-0.80}$	$0.36^{+0.30}_{-0.24}$	$7.31^{+0.20}_{-0.19}$	0.78
362	$64.8^{+10.6}_{-4.1}$	$-0.50^{+1.67}_{-1.54}$	$0.65^{+0.68}_{-0.45}$	$6.57^{+0.63}_{-0.59}$	0.79
1851	$4.0^{+1.5}_{-3.5}$	$-1.35^{+0.56}_{-0.60}$	$2.54^{+1.43}_{-1.40}$	$9.09^{+0.81}_{-0.70}$	0.85
1851	$7.2^{+1.6}_{-1.7}$	$-0.83^{+2.89}_{-1.86}$	$0.87^{+0.96}_{-0.63}$	$10.39^{+0.71}_{-0.65}$	0.85
1851	$11.8^{+2.3}_{-2.9}$	$-0.54^{+1.04}_{-0.98}$	$0.88^{+0.82}_{-0.60}$	$9.54^{+0.46}_{-0.42}$	0.84
1851	$18.5^{+3.8}_{-4.4}$	$0.12^{+0.48}_{-0.47}$	$1.03^{+0.47}_{-0.53}$	$8.60^{+0.26}_{-0.26}$	0.84
1851	$29.4^{+6.0}_{-7.1}$	$0.23^{+0.15}_{-0.15}$	$1.97^{+0.29}_{-0.30}$	$8.24^{+0.17}_{-0.18}$	0.82
1851	$45.5^{+10.7}_{-10.1}$	$-0.06^{+0.15}_{-0.15}$	$1.40^{+0.21}_{-0.21}$	$7.17^{+0.12}_{-0.12}$	0.80
1851	$61.7^{+14.9}_{-5.4}$	$0.31^{+0.56}_{-0.58}$	$0.91^{+0.49}_{-0.50}$	$6.39^{+0.28}_{-0.26}$	0.80
2808	$4.8^{+2.4}_{-4.1}$	$0.21^{+2.27}_{-2.50}$	$1.40^{+1.57}_{-0.97}$	$13.94^{+1.12}_{-1.00}$	0.83
2808	$9.6^{+1.9}_{-2.4}$	$-0.03^{+1.47}_{-1.43}$	$1.49^{+1.57}_{-1.03}$	$13.60^{+0.92}_{-0.89}$	0.83
2808	$15.2^{+3.0}_{-3.7}$	$-0.73^{+0.34}_{-0.35}$	$3.06^{+1.07}_{-1.15}$	$13.33^{+0.56}_{-0.53}$	0.83
2808	$23.8^{+5.0}_{-5.6}$	$-0.67^{+0.29}_{-0.27}$	$2.35^{+0.62}_{-0.63}$	$13.43^{+0.35}_{-0.35}$	0.83
2808	$37.8^{+7.9}_{-9.0}$	$-0.91^{+0.12}_{-0.12}$	$3.50^{+0.41}_{-0.42}$	$12.50^{+0.24}_{-0.22}$	0.83
2808	$54.0^{+18.4}_{-8.3}$	$-0.79^{+0.11}_{-0.11}$	$3.86^{+0.37}_{-0.38}$	$11.33^{+0.22}_{-0.22}$	0.82
3201	$5.8^{+3.1}_{-5.3}$	$2.44^{+1.08}_{-1.47}$	$0.76^{+0.72}_{-0.54}$	$5.36^{+0.50}_{-0.44}$	0.72
3201	$11.8^{+2.4}_{-2.8}$	$0.01^{+1.54}_{-1.59}$	$0.44^{+0.49}_{-0.31}$	$4.60^{+0.33}_{-0.30}$	0.71
3201	$18.7^{+4.0}_{-4.4}$	$-1.00^{+0.58}_{-0.54}$	$0.70^{+0.39}_{-0.41}$	$4.54^{+0.21}_{-0.21}$	0.70
3201	$29.7^{+6.3}_{-7.0}$	$1.16^{+1.57}_{-2.16}$	$0.18^{+0.19}_{-0.13}$	$4.63^{+0.14}_{-0.13}$	0.70
3201	$46.5^{+10.6}_{-10.5}$	$2.97^{+0.57}_{-0.63}$	$0.32^{+0.18}_{-0.18}$	$4.62^{+0.11}_{-0.10}$	0.70
3201	$63.0^{+14.9}_{-6.0}$	$0.27^{+1.93}_{-2.20}$	$0.26^{+0.29}_{-0.18}$	$4.81^{+0.21}_{-0.21}$	0.71
5139	$3.9^{+1.6}_{-3.4}$	$-2.58^{+1.15}_{-0.85}$	$3.67^{+3.58}_{-2.56}$	$22.82^{+1.97}_{-1.74}$	0.73
5139	$7.1^{+1.6}_{-1.6}$	$-2.82^{+0.83}_{-0.73}$	$3.02^{+2.24}_{-1.98}$	$18.23^{+1.25}_{-1.15}$	0.74
5139	$11.4^{+2.4}_{-2.7}$	$1.83^{+0.48}_{-0.46}$	$3.20^{+1.38}_{-1.48}$	$17.57^{+0.79}_{-0.74}$	0.74
5139	$18.2^{+3.7}_{-4.3}$	$-0.20^{+0.25}_{-0.25}$	$4.26^{+0.95}_{-0.98}$	$18.22^{+0.53}_{-0.53}$	0.74
5139	$28.8^{+5.9}_{-6.9}$	$0.17^{+0.45}_{-0.48}$	$1.52^{+0.64}_{-0.74}$	$18.41^{+0.33}_{-0.34}$	0.74
5139	$45.4^{+9.6}_{-10.7}$	$0.34^{+0.12}_{-0.13}$	$3.16^{+0.36}_{-0.36}$	$17.98^{+0.22}_{-0.22}$	0.74
5139	$68.9^{+18.3}_{-13.9}$	$0.15^{+0.22}_{-0.23}$	$2.79^{+0.32}_{-0.30}$	$18.09^{+0.21}_{-0.21}$	0.73
5139	$110.9^{+27.5}_{-23.6}$	$-0.23^{+0.32}_{-0.23}$	$4.27^{+0.95}_{-0.63}$	$16.61^{+0.24}_{-0.22}$	0.72
5139	$177.1^{+42.3}_{-38.7}$	$0.13^{+0.12}_{-0.15}$	$4.33^{+0.38}_{-0.36}$	$14.99^{+0.19}_{-0.18}$	0.69
5139	$267.5^{+57.8}_{-48.2}$	$0.07^{+0.44}_{-0.11}$	$7.21^{+2.90}_{-2.85}$	$13.26^{+0.18}_{-0.17}$	0.67
5904	$3.4^{+1.3}_{-2.8}$	$-2.87^{+0.40}_{-0.39}$	$3.22^{+1.23}_{-1.22}$	$7.33^{+0.81}_{-0.70}$	0.83
5904	$6.1^{+1.4}_{-1.4}$	$-2.47^{+0.88}_{-0.90}$	$1.46^{+1.13}_{-0.99}$	$8.25^{+0.77}_{-0.70}$	0.83
5904	$9.9^{+2.0}_{-2.4}$	$-1.05^{+0.38}_{-0.37}$	$2.16^{+0.78}_{-0.83}$	$7.91^{+0.49}_{-0.46}$	0.83
5904	$15.6^{+3.2}_{-3.7}$	$-0.80^{+1.36}_{-1.21}$	$0.48^{+0.50}_{-0.34}$	$8.02^{+0.35}_{-0.32}$	0.82
5904	$24.6^{+5.2}_{-5.8}$	$-0.51^{+0.21}_{-0.21}$	$1.50^{+0.32}_{-0.31}$	$6.95^{+0.21}_{-0.20}$	0.81
5904	$38.9^{+8.3}_{-9.2}$	$-0.86^{+0.16}_{-0.15}$	$1.51^{+0.22}_{-0.22}$	$6.84^{+0.15}_{-0.14}$	0.79
5904	$55.1^{+20.2}_{-7.8}$	$-1.06^{+0.15}_{-0.14}$	$1.77^{+0.25}_{-0.26}$	$6.79^{+0.16}_{-0.16}$	0.78
6093	$3.7^{+1.7}_{-3.0}$	$0.22^{+0.75}_{-0.79}$	$2.27^{+1.61}_{-1.49}$	$10.47^{+0.86}_{-0.77}$	0.79
6093	$6.9^{+1.8}_{-1.5}$	$2.24^{+1.14}_{-1.58}$	$1.22^{+1.23}_{-0.86}$	$10.42^{+0.84}_{-0.80}$	0.79
6093	$11.5^{+2.3}_{-2.8}$	$0.41^{+2.13}_{-2.54}$	$0.80^{+0.89}_{-0.56}$	$13.16^{+0.66}_{-0.61}$	0.79
6093	$18.1^{+3.9}_{-4.2}$	$-2.52^{+0.31}_{-0.31}$	$2.04^{+0.72}_{-0.74}$	$9.98^{+0.41}_{-0.37}$	0.79
6093	$28.4^{+6.4}_{-6.5}$	$-2.63^{+0.28}_{-0.28}$	$1.65^{+0.51}_{-0.52}$	$9.22^{+0.27}_{-0.28}$	0.78
6093	$44.5^{+10.7}_{-9.7}$	$-2.27^{+0.21}_{-0.21}$	$1.96^{+0.41}_{-0.45}$	$8.29^{+0.26}_{-0.25}$	0.78
6093	$60.5^{+12.9}_{-5.3}$	$-1.73^{+0.34}_{-0.31}$	$2.88^{+1.03}_{-1.02}$	$8.21^{+0.62}_{-0.58}$	0.78
6121	$9.2^{+5.3}_{-8.2}$	$-2.06^{+0.81}_{-0.66}$	$1.71^{+1.17}_{-1.06}$	$6.85^{+0.72}_{-0.64}$	0.74
6121	$19.2^{+3.8}_{-4.7}$	$-1.86^{+3.23}_{-1.29}$	$0.77^{+0.83}_{-0.52}$	$6.57^{+0.69}_{-0.61}$	0.73
6121	$30.2^{+6.4}_{-7.1}$	$-2.66^{+0.69}_{-0.69}$	$1.07^{+0.75}_{-0.67}$	$6.17^{+0.41}_{-0.40}$	0.73
6121	$46.8^{+11.4}_{-10.2}$	$-2.98^{+0.86}_{-0.67}$	$0.71^{+0.52}_{-0.43}$	$5.99^{+0.31}_{-0.31}$	0.73
6254	$3.1^{+1.5}_{-2.8}$	$2.51^{+0.42}_{-0.40}$	$2.48^{+1.02}_{-1.16}$	$5.60^{+0.66}_{-0.59}$	0.73
6254	$6.0^{+1.3}_{-1.4}$	$-2.40^{+0.73}_{-0.71}$	$1.32^{+0.89}_{-0.84}$	$6.41^{+0.50}_{-0.48}$	0.75
6254	$9.6^{+2.0}_{-2.3}$	$2.04^{+0.59}_{-0.54}$	$1.25^{+0.68}_{-0.68}$	$6.82^{+0.43}_{-0.38}$	0.74
6254	$15.2^{+3.2}_{-3.6}$	$-1.18^{+2.36}_{-1.63}$	$0.32^{+0.32}_{-0.23}$	$6.36^{+0.27}_{-0.26}$	0.75
6254	$24.2^{+5.1}_{-5.8}$	$2.62^{+0.61}_{-0.61}$	$0.52^{+0.30}_{-0.30}$	$6.33^{+0.18}_{-0.18}$	0.75
6254	$38.2^{+8.2}_{-8.9}$	$2.12^{+0.49}_{-0.50}$	$0.42^{+0.21}_{-0.22}$	$5.87^{+0.12}_{-0.12}$	0.73
6254	$54.3^{+19.6}_{-7.9}$	$-1.82^{+1.75}_{-1.27}$	$0.17^{+0.19}_{-0.12}$	$5.75^{+0.14}_{-0.13}$	0.74
6266	$3.4^{+1.6}_{-3.1}$	$0.94^{+0.46}_{-0.46}$	$5.07^{+2.27}_{-2.49}$	$15.00^{+1.23}_{-1.03}$	0.83
6266	$6.6^{+1.4}_{-1.5}$	$-1.60^{+0.75}_{-0.77}$	$2.70^{+2.04}_{-1.76}$	$16.08^{+1.01}_{-0.94}$	0.83
6266	$10.6^{+2.2}_{-2.6}$	$2.09^{+1.01}_{-4.41}$	$1.25^{+1.10}_{-0.86}$	$14.58^{+0.61}_{-0.57}$	0.83
6266	$16.7^{+3.5}_{-3.9}$	$1.22^{+1.19}_{-1.28}$	$0.73^{+0.71}_{-0.51}$	$14.65^{+0.39}_{-0.40}$	0.82
6266	$26.7^{+5.4}_{-6.4}$	$1.89^{+0.66}_{-0.65}$	$0.80^{+0.55}_{-0.49}$	$14.17^{+0.26}_{-0.25}$	0.82
6266	$42.0^{+9.0}_{-9.8}$	$1.51^{+0.31}_{-0.33}$	$0.88^{+0.29}_{-0.29}$	$12.66^{+0.16}_{-0.16}$	0.80
6266	$57.4^{+19.3}_{-6.5}$	$1.89^{+0.28}_{-0.27}$	$1.44^{+0.41}_{-0.42}$	$12.00^{+0.23}_{-0.23}$	0.78
6293	$6.1^{+2.9}_{-4.9}$	$-0.52^{+0.56}_{-0.48}$	$2.75^{+1.31}_{-1.34}$	$7.13^{+0.74}_{-0.69}$	0.77
6293	$11.8^{+2.7}_{-2.8}$	$-1.14^{+0.95}_{-0.81}$	$1.69^{+1.38}_{-1.15}$	$7.77^{+0.78}_{-0.74}$	0.77
6293	$18.8^{+4.2}_{-4.3}$	$2.09^{+1.10}_{-1.42}$	$1.02^{+1.07}_{-0.70}$	$6.94^{+0.70}_{-0.63}$	0.77
6293	$28.2^{+8.3}_{-5.2}$	$-1.18^{+0.28}_{-0.28}$	$2.93^{+0.73}_{-0.79}$	$5.41^{+0.54}_{-0.46}$	0.77
6388	$4.8^{+2.2}_{-4.1}$	$-1.89^{+1.08}_{-0.94}$	$2.77^{+2.85}_{-1.92}$	$19.06^{+1.55}_{-1.30}$	0.91
6388	$9.5^{+1.8}_{-2.4}$	$-2.08^{+0.71}_{-0.79}$	$2.63^{+2.12}_{-1.74}$	$19.44^{+1.03}_{-0.93}$	0.91
6388	$15.0^{+3.1}_{-3.6}$	$-1.33^{+0.85}_{-0.83}$	$1.09^{+0.95}_{-0.75}$	$17.38^{+0.46}_{-0.45}$	0.91
6388	$23.5^{+5.1}_{-5.5}$	$-1.23^{+2.79}_{-1.65}$	$0.39^{+0.42}_{-0.27}$	$16.11^{+0.29}_{-0.29}$	0.91
6388	$37.3^{+8.0}_{-8.8}$	$-0.60^{+0.28}_{-0.29}$	$1.17^{+0.33}_{-0.35}$	$13.78^{+0.18}_{-0.18}$	0.89
6388	$53.5^{+18.6}_{-8.2}$	$-0.54^{+0.31}_{-0.31}$	$1.13^{+0.35}_{-0.37}$	$13.16^{+0.20}_{-0.19}$	0.88
6441	$3.1^{+1.8}_{-2.9}$	$-0.73^{+1.90}_{-1.64}$	$1.49^{+1.72}_{-1.02}$	$14.30^{+1.12}_{-0.98}$	0.93
6441	$6.4^{+1.4}_{-1.5}$	$-0.70^{+3.09}_{-2.03}$	$1.85^{+1.75}_{-1.27}$	$19.13^{+1.21}_{-1.11}$	0.93
6441	$10.3^{+2.2}_{-2.4}$	$-0.53^{+0.34}_{-0.34}$	$4.01^{+1.43}_{-1.52}$	$18.23^{+0.72}_{-0.68}$	0.93
6441	$16.4^{+3.4}_{-3.9}$	$0.80^{+1.80}_{-2.33}$	$0.51^{+0.59}_{-0.36}$	$17.13^{+0.40}_{-0.39}$	0.93
6441	$25.8^{+5.5}_{-6.0}$	$2.38^{+1.03}_{-2.87}$	$0.48^{+0.48}_{-0.34}$	$16.33^{+0.29}_{-0.28}$	0.92

Downloaded from https://academic.oup.com/mnras/article-abstract/473/4/5591/4562634
by Liverpool John Moores University user
on 25 January 2018

Table B1 – *continued*

NGC	r (arcsec)	θ_0 (rad)	$v_{\rm rot}$ (km s^{-1})	$\sigma_{\rm r}$ (km s^{-1})	$M_{\rm eff.}$ ($M_\odot$)
6441	$40.7^{+9.0}_{-9.3}$	$2.51^{+0.99}_{-1.25}$	$0.37^{+0.34}_{-0.25}$	$14.96^{+0.19}_{-0.19}$	0.92
6441	$56.4^{+17.9}_{-6.7}$	$-1.97^{+4.58}_{-1.07}$	$0.65^{+0.50}_{-0.43}$	$14.31^{+0.26}_{-0.26}$	0.91
6522	$5.4^{+2.6}_{-4.9}$	$1.76^{+1.08}_{-1.07}$	$1.58^{+1.52}_{-1.11}$	$9.31^{+1.00}_{-0.84}$	0.79
6522	$10.7^{+2.0}_{-2.7}$	$-2.75^{+0.52}_{-0.50}$	$2.61^{+1.37}_{-1.33}$	$9.53^{+0.81}_{-0.74}$	0.79
6522	$16.7^{+3.5}_{-3.9}$	$0.83^{+0.83}_{-1.04}$	$1.07^{+0.88}_{-0.73}$	$9.27^{+0.56}_{-0.51}$	0.79
6522	$26.1^{+6.0}_{-5.8}$	$-0.75^{+0.77}_{-0.64}$	$1.13^{+0.73}_{-0.70}$	$9.38^{+0.45}_{-0.42}$	0.78
6522	$35.5^{+7.8}_{-3.4}$	$-0.83^{+1.70}_{-1.49}$	$1.00^{+1.04}_{-0.69}$	$9.10^{+0.75}_{-0.68}$	0.78
6541	$4.0^{+1.9}_{-3.3}$	$1.24^{+1.52}_{-1.94}$	$1.28^{+1.53}_{-0.89}$	$11.53^{+1.15}_{-1.04}$	0.78
6541	$7.8^{+1.6}_{-1.9}$	$-1.35^{+2.32}_{-1.51}$	$0.98^{+1.07}_{-0.68}$	$10.92^{+0.82}_{-0.79}$	0.78
6541	$12.2^{+2.6}_{-2.9}$	$1.31^{+1.60}_{-2.55}$	$0.61^{+0.65}_{-0.43}$	$10.34^{+0.52}_{-0.47}$	0.77
6541	$19.5^{+4.1}_{-4.6}$	$-1.61^{+0.69}_{-0.73}$	$0.73^{+0.54}_{-0.46}$	$8.07^{+0.30}_{-0.30}$	0.76
6541	$30.8^{+6.6}_{-7.2}$	$-1.76^{+0.16}_{-0.18}$	$2.00^{+0.36}_{-0.35}$	$7.59^{+0.23}_{-0.23}$	0.75
6541	$47.0^{+12.2}_{-9.6}$	$-1.74^{+0.12}_{-0.12}$	$2.40^{+0.26}_{-0.27}$	$6.84^{+0.18}_{-0.18}$	0.74
6541	$63.8^{+11.1}_{-4.6}$	$-1.49^{+0.25}_{-0.27}$	$2.95^{+0.79}_{-0.76}$	$6.62^{+0.52}_{-0.50}$	0.74
6656	$3.0^{+1.6}_{-2.5}$	$1.94^{+1.16}_{-1.29}$	$1.37^{+1.34}_{-0.95}$	$9.16^{+0.92}_{-0.91}$	0.68
6656	$5.9^{+1.3}_{-1.4}$	$-0.99^{+0.32}_{-0.33}$	$4.05^{+1.27}_{-1.34}$	$9.66^{+0.79}_{-0.71}$	0.69
6656	$9.5^{+2.0}_{-2.3}$	$1.65^{+1.42}_{-2.09}$	$0.64^{+0.72}_{-0.45}$	$9.92^{+0.58}_{-0.51}$	0.69
6656	$15.2^{+3.1}_{-3.7}$	$-1.86^{+1.46}_{-1.15}$	$0.53^{+0.59}_{-0.38}$	$9.66^{+0.39}_{-0.38}$	0.70
6656	$23.9^{+5.0}_{-5.6}$	$-0.33^{+0.89}_{-0.92}$	$0.54^{+0.40}_{-0.35}$	$9.62^{+0.25}_{-0.23}$	0.70
6656	$37.8^{+8.1}_{-8.9}$	$-1.65^{+0.47}_{-0.45}$	$0.61^{+0.31}_{-0.32}$	$9.66^{+0.16}_{-0.17}$	0.69
6656	$54.2^{+18.6}_{-8.3}$	$-1.69^{+0.32}_{-0.31}$	$0.89^{+0.30}_{-0.30}$	$9.48^{+0.16}_{-0.16}$	0.69
6681	$3.7^{+1.9}_{-3.2}$	$2.54^{+0.65}_{-0.75}$	$2.04^{+1.47}_{-1.30}$	$8.45^{+0.81}_{-0.75}$	0.78
6681	$7.5^{+1.5}_{-1.8}$	$1.23^{+1.36}_{-1.47}$	$0.86^{+0.88}_{-0.62}$	$8.01^{+0.62}_{-0.59}$	0.77
6681	$11.9^{+2.4}_{-2.8}$	$0.29^{+1.27}_{-1.38}$	$0.50^{+0.47}_{-0.35}$	$6.60^{+0.35}_{-0.33}$	0.76
6681	$18.7^{+4.1}_{-4.3}$	$1.04^{+1.27}_{-1.41}$	$0.31^{+0.32}_{-0.22}$	$6.14^{+0.21}_{-0.21}$	0.74
6681	$28.3^{+7.7}_{-5.6}$	$1.54^{+0.72}_{-0.73}$	$0.40^{+0.29}_{-0.26}$	$5.39^{+0.17}_{-0.16}$	0.73
6681	$38.8^{+5.4}_{-2.8}$	$1.77^{+1.33}_{-2.72}$	$0.57^{+0.64}_{-0.40}$	$5.20^{+0.57}_{-0.53}$	0.73
6752	$3.9^{+2.0}_{-3.3}$	$-0.85^{+1.91}_{-1.67}$	$0.92^{+1.03}_{-0.65}$	$8.37^{+0.74}_{-0.67}$	0.80
6752	$7.8^{+1.5}_{-1.9}$	$1.48^{+0.61}_{-0.61}$	$2.11^{+1.31}_{-1.23}$	$9.72^{+0.74}_{-0.64}$	0.79
6752	$12.4^{+2.6}_{-2.9}$	$-0.57^{+2.46}_{-1.96}$	$0.46^{+0.51}_{-0.33}$	$8.97^{+0.42}_{-0.39}$	0.77
6752	$19.7^{+4.1}_{-4.7}$	$-2.90^{+1.00}_{-0.76}$	$0.53^{+0.44}_{-0.35}$	$7.62^{+0.25}_{-0.23}$	0.75
6752	$31.0^{+6.7}_{-7.2}$	$0.30^{+1.54}_{-1.64}$	$0.23^{+0.24}_{-0.16}$	$7.62^{+0.17}_{-0.16}$	0.74
6752	$47.6^{+12.2}_{-9.9}$	$-2.85^{+1.42}_{-0.72}$	$0.26^{+0.22}_{-0.18}$	$7.22^{+0.13}_{-0.13}$	0.72
6752	$64.5^{+11.4}_{-4.7}$	$2.61^{+0.52}_{-0.50}$	$1.34^{+0.66}_{-0.67}$	$7.68^{+0.41}_{-0.37}$	0.72
7078	$2.9^{+1.5}_{-2.6}$	$-3.03^{+0.38}_{-0.35}$	$5.66^{+2.35}_{-2.48}$	$14.00^{+1.19}_{-1.06}$	0.76
7078	$5.7^{+1.2}_{-1.4}$	$-1.69^{+0.61}_{-0.62}$	$2.87^{+1.64}_{-1.63}$	$12.78^{+0.96}_{-0.86}$	0.76
7078	$9.1^{+1.8}_{-2.2}$	$-0.21^{+0.85}_{-0.81}$	$1.60^{+1.21}_{-1.03}$	$12.48^{+0.65}_{-0.60}$	0.76
7078	$14.4^{+3.0}_{-3.4}$	$1.94^{+1.15}_{-1.27}$	$0.72^{+0.70}_{-0.50}$	$12.73^{+0.44}_{-0.43}$	0.76
7078	$22.7^{+4.9}_{-5.3}$	$2.55^{+0.98}_{-2.20}$	$0.42^{+0.42}_{-0.29}$	$11.20^{+0.28}_{-0.27}$	0.75
7078	$36.0^{+7.7}_{-8.4}$	$2.59^{+0.21}_{-0.22}$	$1.51^{+0.34}_{-0.33}$	$10.17^{+0.20}_{-0.19}$	0.75
7078	$52.2^{+17.1}_{-8.4}$	$2.54^{+0.14}_{-0.14}$	$2.16^{+0.31}_{-0.33}$	$8.98^{+0.20}_{-0.20}$	0.74
7089	$3.5^{+1.9}_{-3.4}$	$-0.41^{+1.03}_{-1.02}$	$2.02^{+1.96}_{-1.42}$	$12.35^{+1.02}_{-0.97}$	0.80
7089	$7.1^{+1.5}_{-1.7}$	$1.62^{+0.78}_{-0.76}$	$1.99^{+1.53}_{-1.33}$	$10.83^{+0.81}_{-0.76}$	0.80
7089	$11.4^{+2.3}_{-2.7}$	$1.33^{+0.80}_{-0.80}$	$1.06^{+0.86}_{-0.71}$	$10.25^{+0.43}_{-0.43}$	0.80
7089	$17.9^{+3.8}_{-4.2}$	$0.76^{+0.31}_{-0.30}$	$1.85^{+0.56}_{-0.56}$	$10.64^{+0.32}_{-0.31}$	0.80
7089	$28.5^{+5.9}_{-6.8}$	$0.75^{+0.11}_{-0.11}$	$3.24^{+0.33}_{-0.34}$	$9.75^{+0.20}_{-0.21}$	0.79
7089	$44.4^{+10.0}_{-10.0}$	$0.69^{+0.07}_{-0.07}$	$3.44^{+0.25}_{-0.24}$	$8.96^{+0.14}_{-0.14}$	0.78

Table B1 – *continued*

NGC	r (arcsec)	θ_0 (rad)	$v_{\rm rot}$ (km s^{-1})	$\sigma_{\rm r}$ (km s^{-1})	$M_{\rm eff.}$ ($M_\odot$)
7089	$60.3^{+16.4}_{-5.9}$	$0.80^{+0.13}_{-0.12}$	$3.67^{+0.43}_{-0.45}$	$8.18^{+0.27}_{-0.27}$	0.78
7099	$2.9^{+1.4}_{-2.5}$	$-1.81^{+2.95}_{-1.37}$	$1.02^{+1.03}_{-0.71}$	$8.13^{+0.79}_{-0.71}$	0.76
7099	$5.7^{+1.2}_{-1.4}$	$-2.53^{+1.90}_{-0.98}$	$1.02^{+1.01}_{-0.71}$	$7.51^{+0.62}_{-0.59}$	0.75
7099	$9.0^{+2.0}_{-2.0}$	$1.36^{+1.28}_{-1.38}$	$0.56^{+0.59}_{-0.39}$	$6.54^{+0.43}_{-0.40}$	0.75
7099	$14.4^{+3.1}_{-3.4}$	$2.59^{+0.94}_{-1.23}$	$0.43^{+0.42}_{-0.29}$	$6.23^{+0.26}_{-0.26}$	0.74
7099	$22.8^{+5.0}_{-5.2}$	$-1.71^{+0.72}_{-0.73}$	$0.46^{+0.31}_{-0.31}$	$5.77^{+0.18}_{-0.17}$	0.73
7099	$35.8^{+8.3}_{-8.0}$	$-1.84^{+0.75}_{-0.76}$	$0.33^{+0.24}_{-0.21}$	$5.50^{+0.15}_{-0.13}$	0.72
7099	$52.9^{+17.1}_{-8.8}$	$-1.81^{+0.84}_{-0.84}$	$0.30^{+0.24}_{-0.19}$	$5.22^{+0.16}_{-0.14}$	0.71

APPENDIX C: BIAS ESTIMATES FOR THE (v/σ) AND $\lambda_{\rm R}$ PROFILES

As mentioned above in Section 5.3, the values obtained for (v/σ) and $\lambda_{\rm R}$ have to be corrected for biases introduced by the finite accuracy of the data. The reason for this is that any deviations from the mean velocity that enter equations (5) and (6), regardless of whether they are caused by cluster rotation or statistic scatter, contribute to the final result.

To estimate the contribution of the statistic scatter to our values for (v/σ) and $\lambda_{\rm R}$, we made the following approach. We used the same Voronoi bins depicted in Figs 5 and A1 and assigned each bin a new mean velocity under the assumption that the rotation velocity scales linearly with radius, i.e. $v_{\rm rot}(r) = \alpha r$. From these data, we determined unbiased values for (v/σ) and $\lambda_{\rm R}$. Then we added scatter to the simulated rotation field, according to the noise estimates we obtained for each Voronoi bin from our data and recalculated (v/σ) and $\lambda_{\rm R}$. The latter values are biased to high values because of the additional noise distribution. We repeated this analysis for different velocity gradients α, leading to a relation between the biased values and the intrinsic ones that is displayed in Fig. C1 for the example of NGC 2808. Using this relation, we can correct the value measured on the real data (the horizontal line in Fig. C1) to get an unbiased measurement (the vertical dashed line) and a corresponding uncertainty interval (the dotted vertical lines). The uncertainties were obtained by rerunning the simulation $N = 100$ times for each value of α.

In Fig. C1, the bias correction is displayed for two different types of binning. In upper panels, we used the original Voronoi bins as displayed in Figs 5 and A1. The results displayed in the bottom panels were obtained by creating new two-dimensional maps from the radial profiles as outlined in Section 5.3. It is obvious that for this approach, the biases are significantly reduced because of the smaller uncertainties per Voronoi bin. We observed a similar behaviour for all of our clusters; hence, we decided to use the maps created from the radial profiles. It is further visible in Fig. C1 that the bias was stronger for the (v/σ) measurements than it was for the $\lambda_{\rm R}$ measurements. The reason for this is likely the weighting with projected radius when determining $\lambda_{\rm R}$, see equation (6), which enhances the rotation signal compared to random scatter. For this reason, we decided to prefer the values obtained for $\lambda_{\rm R}$ over those obtained for (v/σ) (keeping in mind that both values gave very similar results).

Downloaded from https://academic.oup.com/mnras/article-abstract/473/4/5591/4562634
by Liverpool John Moores University user
on 25 January 2018

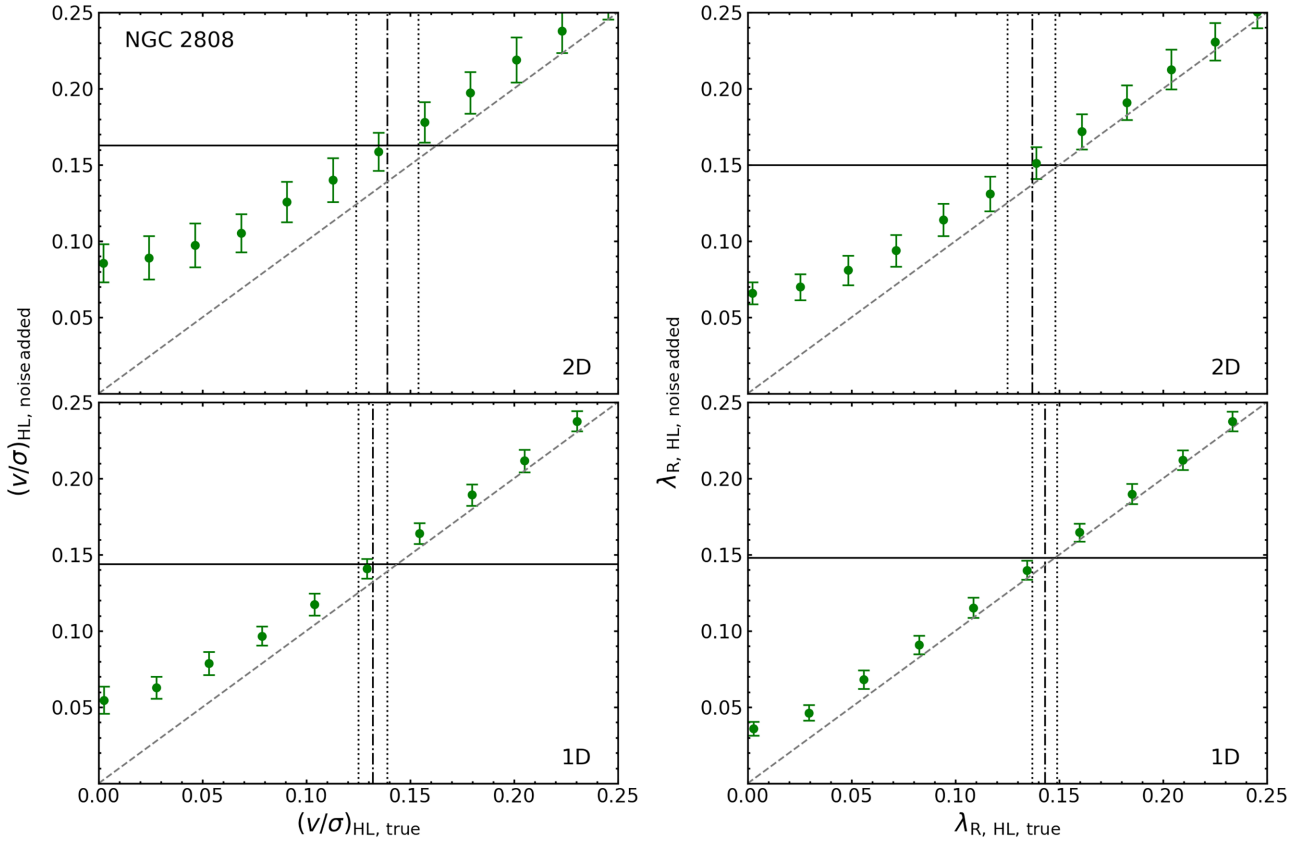

Figure C1. Bias correction applied when determining $(v/\sigma)_{\rm HL}$ (left) or $\lambda_{\rm R,\,HL}$ (right), using the example of NGC 2808. The top panels show the results obtained on the original 2D grid; the bottom panels show the results obtained when creating a new grid from the 1D radial profiles. Each plot shows the recovered value (after adding noise) as a function of the intrinsic one (without noise). Green circles indicate the results from our simulations. The solid horizontal line is the value measured from the actual data; the dashed and dotted vertical lines provide the value and the 1σ uncertainty interval after correction for the noise bias.

This paper has been typeset from a TEX/LATEX file prepared by the author.

Downloaded from https://academic.oup.com/mnras/article-abstract/473/4/5591/4562634
by Liverpool John Moores University user
on 25 January 2018